SIAM J. Applied Dynamical Systems
Vol. 24, No. 1, pp. 187–218

# Phase-Based Reduced Order Models for Parabolic and Elliptic Bursting Neurons[*]

Dan Wilson[†]

**Abstract.** While many well-established approaches exist for phase-based reduced order modeling of tonically firing neurons, comparatively few general approaches exist for the consideration of bursting neurons in a reduced order setting. Many formal analysis strategies exploit the separation of fast and slow timescales present in most bursting neurons, but these approaches are typically ill-suited to consider emergent behavior resulting from inter-neuron coupling or other external perturbations. This work considers the development and analysis of two different model order reduction approaches valid for two different topological classes of bursting neurons. For parabolic bursters, a persistent invariant circle allows for the relatively straightforward application of the extended phase reduction approach. For elliptic bursters, the perturbed dynamics can be considered relative to a carefully chosen set of reference trajectories. Mathematical analysis and accompanying numerical illustrations demonstrate the utility of the proposed approaches.

**Key words.** bursting neurons, phase model, model order reduction, computational neuroscience

**MSC codes.** 34E10, 37C27, 92C20, 34C15

**DOI.** 10.1137/23M1625317

## 1. Introduction.

From a biophysical perspective, neural spiking can be explained in terms of the complex interplay between ionic currents, gating variables, and synaptic neurotransmitters [12], [9], [22]. These features can be combined numerically to construct conductance-based neural models with model parameters tuned to match experimental observations. Such models can replicate a wide variety of neural spiking behaviors, but given the complexity of most conductance-based neural models, it is often desirable to work with simplified models. For instance, integrate and fire neuron models [49], [46] eschew the spiking dynamics to focus on the subthreshold behavior with a predefined spiking threshold and possibly a refractory period. By contrast, for tonic (repetitively firing) neurons, a coordinate change to phase variables using isochrons [58], [14] yields a reduction of dimensionality and ultimately allows for the implementation of weakly coupled oscillator theory [25], [18] to study the aggregate behaviors of weakly perturbed and weakly interacting neurons [50] [4], [56], [17].

While phase-based reduction techniques have allowed for a greater understanding of the behavior of coupled, tonically firing neurons, they are typically unable to accommodate bursting neurons, i.e., those that transition between tonic firing and quiescence [22]. Bursting neurons are ubiquitous in the central nervous system, providing the building blocks that comprise

---

[*] Received by the editors December 19, 2023; accepted for publication by J. Rubin September 19, 2024; published electronically January 9, 2025.
https://doi.org/10.1137/23M1625317
**Funding:** This material is based upon work supported by the National Science Foundation (NSF) under grant CMMI-2140527.

[†] Department of Electrical Engineering and Computer Science, University of Tennessee, Knoxville, TN 37996 USA (dwilso81@utk.edu).

central pattern generators [28], [29], [6], including those found in animal respiration cycles [45], [33], [35]. Bursting neurons can typically be characterized by a fast-slow timescale separation of the form [22, 12]

$$\begin{aligned} \dot{x} &= f(x, y), \\ \dot{y} &= \epsilon g(x, y), \end{aligned} \tag{1}$$

where $x \in \mathbb{R}^m$ are the fast variables responsible for spiking, $y \in \mathbb{R}^k$ are the slow variables that modulate spiking, $f$ and $g$ give the dynamics of the fast and slow variables, respectively, and $0 < \epsilon \ll 1$. Standard phase-based analysis is usually insufficient for bursting neurons because the underlying assumptions break down when the state transitions between attractors (i.e., between tonic firing and quiescence) [22]. Indeed, existing phase-based reduction techniques applied to bursting neuron cycles result in reduced order models with considerable phase sensitivity [44], [30], precluding practical use as a tool for understanding coupled oscillations. Additionally, while the timescale separation in (1) allows for analysis of the fast equations $\dot{x} = f(x, y)$ in the limit that $\epsilon \to 0$, it can be hard to accommodate coupling between neurons with these formulations [3], [53], [38]. Other methods including averaging [42] or the equivalent voltage method [24], [2] can be used to capture the dynamics of the slow variables, but their underlying assumptions also break down near bifurcations.

In direct contrast with tonically firing neurons, where phase-based reduced order modeling can be used to understand emergent behaviors in relation to the underlying biology (ionic currents, neurotransmitters, etc.), reduced order modeling techniques for understanding the behaviors of coupled and perturbed bursting neurons are insufficiently developed. Consequently, studies of coupled bursting neurons are often confined to low-dimensional, phenomenological models [1], [7], [48], [43], [40], [41], [19]. While phenomenological models are convenient for mathematical analysis, they generally do not preserve salient aspects of the physiology of the neuron (e.g., specific ionic currents, ionic concentrations), which is an important consideration in many applications. With this in mind, the proposed approach offers a framework to analyze physiologically detailed bursting neurons using a reduced order coordinate framework, sidestepping the need to resort to phenomenological representations. Two common topological classes of neurons are considered in this work. The first is parabolic bursting, for which spiking begins and ends as a result of a saddle node on an invariant circle bifurcation. The second is elliptic bursting, whereby resting stability is lost through a subcritical Hopf bifurcation and the subsequent transition back to quiescence results from a fold limit cycle bifurcation [22], [12]. In this work, different strategies are required for reduction of parabolic and elliptic bursters because different bifurcations underlie their dynamical behavior.

The organization of this paper is as follows: Section 2 provides necessary background on existing phase-based reduced order modeling strategies that are relevant to the methods considered in this work. Section 3 investigates a model order reduction approach for parabolic bursters. For this topological class of neuron, the persistence of the invariant circle during both firing and quiescence ultimately allows for the use of the extended phase reduction approach presented in [26]. Section 4 investigates a model order reduction approach for elliptic bursters. Here, by considering the system relative to a continuous set of carefully chosen reference trajectories parameterized by a time-like and an amplitude-like variable, it is possible to accurately capture the transition between spiking and quiescence. Brief remarks are given about the proposed methodology to the application of fold/homoclinic (square wave) bursters in section 5. Concluding remarks are provided in section 6.

## 2. Background.

**2.1. Phase reduction.** Consider the dynamics of a conductance-based neuron of the general form

$$\begin{aligned} C_m\dot{V} &= I_{\text{ion}}(V,a,p_0) + I_{\text{ext}}(\mu), \\ \dot{a} &= f_a(V,a,p_0), \end{aligned} \tag{2}$$

where $V \in \mathbb{R}$ is the transmembrane potential, $C_m$ is a membrane capacitance, $a \in \mathbb{R}^{N-1}$ is a collection of auxiliary variables (ionic concentrations, gating variables, etc.), $I_{\text{ion}}$ is a collection of ionic currents, and $I_{\text{ext}}$ is an external ionic current (synaptic current, externally applied current, etc.) that is a function of $\mu \in \mathbb{R}^{\psi}$. Here, $p_0 \in \mathbb{R}^M$ is also explicitly included to highlight the effect of a subset of the system parameters. Note that the formulation (2) is different from the fast-slow formulation from (1). To proceed, let $x = \begin{bmatrix} V & a^T \end{bmatrix}^T \in \mathbb{R}^N$ comprise the state of the full system (2). For tonically firing neurons, i.e., those with that fire at regular intervals, phase reduction [12, 22, 37, 31] is an often used strategy to reduce the dimension and complexity of (2). To employ this strategy, suppose that (2) has a $T(p_0)$-periodic, stable limit cycle $x^{\gamma}_{p_0}$ when $\mu = \vec{0}$ where $\vec{0}$ is an appropriately sized vector of zeros. The phase, $\theta \in [0, 2\pi)$, can be defined for all states $x \in x^{\gamma}_{p_0}$ with $\theta$ scaled so that $\frac{d\theta}{dt} = 2\pi/T(p_0) \equiv \omega(p_0)$ when $\mu = \vec{0}$. Isochrons [14], [57] are typically used to extend the definition of phase to the basin of attraction of the limit cycle as follows: letting $\theta_1$ be the phase associated with some $b \in x^{\gamma}_{p_0}$, the $\theta_1$ isochron is the set of all $c$ for which

$$\lim_{t\to 0} ||\phi(t,b) - \phi(t,c)|| = 0, \tag{3}$$

where $\phi(t,x)$ denotes the flow of (2) subject to $\mu = \vec{0}$ and $||\cdot||$ can be any vector norm. Phase reduction of (2) can be implemented by changing to phase coordinates

$$\dot{\theta} = \omega(p_0) + Z_R(\theta,p_0)\mu. \tag{4}$$

Here, $Z_R(\theta,p_0) = \frac{\partial\theta}{\partial V}\frac{\partial I_{\text{ext}}}{\partial\mu}$ is often referred to as the phase response curve where the partial derivatives are evaluated at $x^{\gamma}_{p_0}(\theta)$ and at $\mu = \vec{0}$. When using (4), an estimate of the state can be obtained according to $x(t) \approx x^{\gamma}_{p_0}(\theta(t))$. In the identification of $Z_R(\theta,p_0)$ from (4), when the model equations (2) are available, it is generally convenient to compute $\frac{\partial\theta}{\partial x}$ (which contains $\frac{\partial\theta}{\partial V}$) using the adjoint method [5]. In an experimental setting, it is also possible to use the direct method [34], which entails giving a perturbation at a known phase, inferring the change in phase, repeating the process at different phases, and fitting a curve to the resulting data to infer $Z_R$.

**2.2. Extended phase reduction.** For the phase reduction from (4), the partial derivatives that comprise $Z_R(\theta,p_0)$ are evaluated at $x^{\gamma}_{p_0}(\theta)$. As such, its accuracy suffers when the state $x$ is far from $x^{\gamma}_{p_0}(\theta)$. In practice, this leads to the caveat that phase reduction of the form (4) is only guaranteed to be valid when $\mu(t)$ is small relative to the nonunity Floquet multipliers associated with the periodic orbit so that $x(t) - x^\gamma_{p_0}(\theta)$ stays relatively small. Reference [26] presented an extension to standard phase reduction theory for use when the input can be decomposed as the summation of a small amplitude component with a slowly varying component. Summarizing the results of [26] here, consider a general dynamical system of the form

$$\dot{x} = F(x, \mu), \tag{5}$$

where $x \in \mathbb{R}^N$ is the state and $\mu \in \mathbb{R}^\psi$ is an input. When taking $\mu$ to be constant, suppose that (5) has a stable limit cycle $x^\gamma_\mu(\theta)$ for $\mu \in A$, where $A$ is an open subset of $\mathbb{R}^\psi$. Let $T(\mu)$ be the associated period with $\omega(\mu) = 2\pi/T(\mu)$ being the natural frequency. The limit cycle $x^\gamma_\mu(\theta)$ can be parameterized by a phase $\theta \in [0, 2\pi)$ using isochrons as defined in (3). Assume that $x^\gamma_\mu(\theta)$ is continuous with respect to $\theta$ and $\mu \in A$. Note that the isochrons of $x^\gamma_\mu(\theta)$ are unique up to a constant shift; in practice it is possible to disambiguate the phase shift between limit cycles, for instance, by defining a Poincaré section transverse to the set of limit cycles and defining the crossing of this section to correspond to a level set of phase between limit cycles. With this in mind, an extended phase can be defined, $\theta(x, \mu)$, that is a function of both the state and the input. When $\mu$ is allowed to vary in time, suppose that it can be decomposed according to

$$\mu(t) = q(\epsilon t) + \sigma p(t), \tag{6}$$

where $\epsilon$ and $\sigma$ are both sufficiently small and that $q(\epsilon t)$ is continuously differentiable with respect to $t$. Reference [26] showed that the dynamics of the extended phase are

$$\dot{\theta} = \omega(q(\epsilon t)) + \sigma Z(\theta, q(\epsilon t))p(t) + \epsilon D(\theta, q(\epsilon t))\dot{q}(\epsilon t) + O(\epsilon^2, \sigma^2, \epsilon\sigma), \tag{7}$$

where

$$\begin{aligned} Z(\theta, q(\epsilon t)) &= \frac{\partial \theta}{\partial x}^T \frac{\partial F}{\partial \mu}, \\ D(\theta, q(\epsilon t)) &= -\frac{\partial x^\gamma_\mu}{\partial \mu}^T \frac{\partial \theta}{\partial x}, \\ x(t) &= x^\gamma_{q(\epsilon t)}(\theta) + O(\epsilon, \sigma). \end{aligned} \tag{8}$$

Above, all partial derivatives are evaluated at $x = x^\gamma_\mu$ and $\mu = q(\epsilon t)$. As with standard phase reduction (4), $Z(\theta, \mu)$ can be computed individually for each limit cycle $x^\gamma_\mu$ using the adjoint method. The terms $\frac{\partial x^\gamma_\mu}{\partial \mu}$ can be obtained using finite difference approximations with knowledge of each limit cycle and can also be computed with methods discussed in [52]. This approach was further extended in [54] to consider both phase and amplitude coordinates, ultimately eliminating the need to decompose $\mu(t)$ in terms of a slowly varying and small amplitude signal.

## 3. Reduced order models for Circle/Circle (parabolic) bursters.

For Circle/Circle bursting (i.e., parabolic bursting), tonic spiking begins when a stable quiescent state loses stability via a saddle-node on an invariant circle (SNIC) bifurcation. Spiking subsequently ends through another SNIC bifurcation. Typically, autonomous Circle/Circle bursting can be characterized according to a fast-slow timescale separation of the form (1) where the slow dynamics have at least two variables. In this section, a 6-variable model from [8] is considered with associated equations provided in Appendix A. In the context of fast-slow decomposition from (1), the transmembrane voltage ($V$) gating variables ($n$ and $h$) and intracellular calcium concentration ($[\mathrm{Ca_i}]$) are taken to be part of the fast equations. The remaining concentrations $[\mathrm{Na}]_\mathrm{o}$ and $[\mathrm{K}]_\mathrm{i}$ comprise the slow equations. Using the dissection method [38], one can hold the slow variables constant and examine the resulting behavior of the fast equations. Applying the dissection method, as shown in panel D of Figure 1, when $I_\mathrm{ext} = 0$, the dashed line separates regions of tonic firing and quiescence through a curve of SNIC bifurcations. Panels A–C show the voltage and slow variable ion concentrations during a simulation of the full model (A1) when $I_\mathrm{ext} = 0$. Plotting the potassium concentration against the sodium concentration in panel D, one finds that the line of SNIC bifurcations accurately separates the firing from the quiescent regime.

**3.1. Forced Circle/Circle bursting.** The goal here is to consider the dynamics of (A1) with a reduced order model that accurately captures the transitions between quiescence and bursting. To do so, consider the system (A1) in terms of its fast-slow decomposition of the form (1). For the moment, we will take $\dot{y} = 0$ so that $y = y_0$ is constant. The system can also be represented in the form of (2),

$$\begin{aligned} C_m\dot{V} &= I_\mathrm{ion}(V,a,y) + I_\mathrm{ext}(\mu), \\ \dot{a} &= f_a(V,a,y), \end{aligned} \tag{9}$$

where $y$ takes the place of the parameter $p_0$ from (2). Recall that $I_\mathrm{ion}$ is comprised of all ionic currents of an individual neuron and $I_\mathrm{ext}$ is some external transmembrane current source that could, for instance, account for the influence of synaptic current or a direct current injection from a patch clamp. For concreteness, consider $y_0 = \left[[\mathrm{Na}]_\mathrm{o} \quad [\mathrm{K}]_\mathrm{i}\right]^T = [18.5 \quad 6.5]^T$ mM. Considering panel D of Figure 1, when $I_\mathrm{ext} = 0$ this is in the quiescent regime; in this case the SNIC bifurcation occurs at $I_\mathrm{ext} = 0.263\ \mu\mathrm{A/cm}^2$. In order to apply the phase reduction,

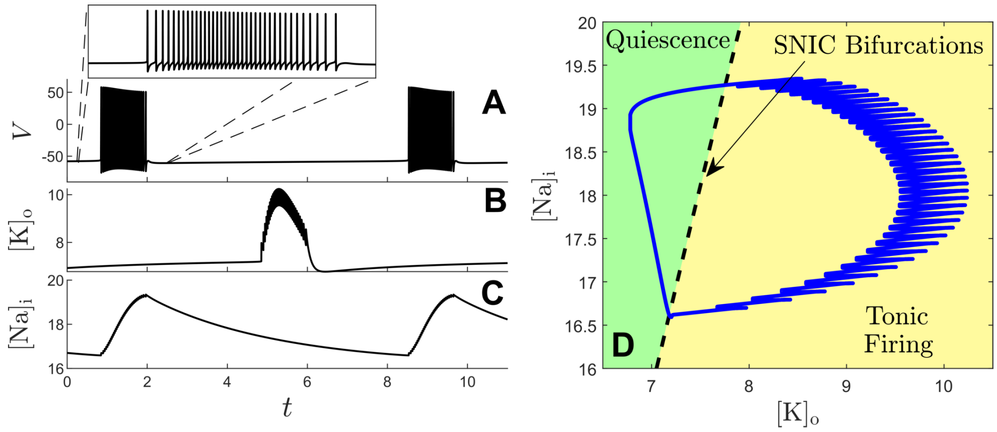

**Figure 1.** *For simulations of the parabolic bursting model from (A1), panels A, B, and C show traces of the transmembrane voltage (in mV), extracellular potassium, and intracellular sodium concentrations (in mM), respectively, during a full bursting cycle. Panel D shows the potassium and sodium concentrations plotted over time with the active phase (tonic firing) occurring on the right side of the line of SNIC bifurcations.*

consider the periodic orbit that results from taking $I_{\text{ext}}(\mu) = 0.5 + \mu$. For this periodic orbit, it is straightforward to compute the phase reduction of the form (4)

$$\dot{\theta} = \omega(y_0) + Z_R(\theta, y_0)(I_{\text{ext}}(t) - 0.5). \tag{10}$$

As shown in Appendix C, when using the phase reduction (10), the SNIC bifurcation is preserved in the transition to the phase reduced model with the bifurcation occurring for the same value of the input. Indeed, results in Figure 2 show nearly indistinguishable results for two different inputs. Applying $I_{\text{ext}}(t) = 2\sin(2\pi t/100)$ as shown in panel C yields regular 3-spike bursts as shown in panel B. Here, for the reduced order model $V(\theta) = x^{\gamma}_{y_0}(\theta)$. Panel A shows the corresponding phase during the simulation. Similar results are shown in panels D–F. In this case, $I_{\text{ext}}$ is obtained as follows: random numbers between $-2.5$ and 1.5 are chosen from a uniform distribution and held constant over a 20 ms time interval, and the resulting signal is smoothed using spline interpolation. Results from Figure 2 illustrate that standard phase reduction of the form (4) provides an adequate 1-dimensional representation of the full order dynamics. Note that a Gaussian white noise process can also be used in place of $I_{\text{ext}}(t)$; in this case, the reduced order model also accurately captures the spiking times in the full order model (results not shown).

The standard, 1-dimensional phase reduction (4) is guaranteed to be accurate in the limit in which the perturbations are infinitesimally small. In the the next section, a case where the slow variables are allowed to change will be considered; for that model the standard phase reduction (4) is insufficient, necessitating the use of the extended phase reduction (7).

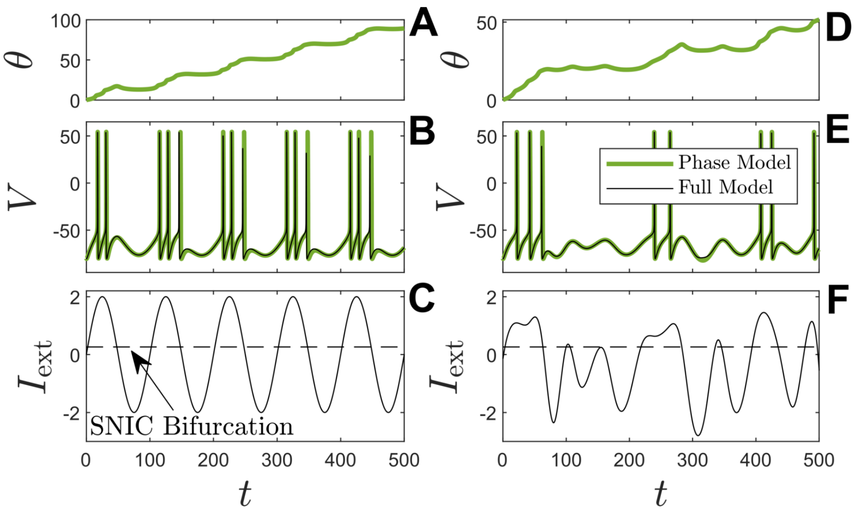

**Figure 2.** *For the model (A1), the slow variables* $[\mathrm{Na}]_{\mathrm{o}}$ *and* $[\mathrm{K}]_{\mathrm{i}}$ *are held constant, and the fast equations are analyzed using phase reduction yielding the model (10). For the sinusoidal external current shown in panel C, outputs for the full and reduced order models are nearly identical, as shown in panel B. Panel A gives the corresponding value of phase during simulations of the reduced order model. The horizontal dashed line in panel C denotes the value at which the SNIC bifurcation occurs with the reduced order model transitioning freely between firing and quiescence. Panels D–F give a similar result with a different input that is chosen randomly as described in the text.*

**3.2. Circle/Circle bursting with slow variable dynamics.** Results from section 3.1 consider the model (A1) in the limit in which the slow variables are constant. Here, the slow variables will be allowed to change, necessitating the use of the extended phase reduction described in section 2.2. To formulate this problem in this manner, the model (A1) can be written as

$$\dot{x} = F(x, \mu), \tag{11}$$

where $x = \begin{bmatrix} V & n & h & [\mathrm{Ca}]_\mathrm{i} \end{bmatrix}^T$ are the fast variables and $\mu = \begin{bmatrix} I_\mathrm{ext} & [\mathrm{Na}]_\mathrm{o} & [\mathrm{K}]_\mathrm{i} \end{bmatrix}^T$ is comprised of the external current input and the slow variables. Such a system could describe, for instance, a neuron where the bursting is mediated by the slow variable dynamics that also receives an additional synaptic current from an external source. Because $[\mathrm{Na}]_\mathrm{o}$ and $[\mathrm{K}]_\mathrm{i}$ are slow variables, provided $I_\mathrm{ext}(t)$ is small in magnitude, it can be decomposed in the same form as (6),

$$\mu(t) = \underbrace{\begin{bmatrix} 0 \\ [\mathrm{Na}]_\mathrm{o}(t) \\ [\mathrm{K}]_\mathrm{i}(t) \end{bmatrix}}_{\text{slowly varying}} + \underbrace{\begin{bmatrix} I_\mathrm{ext}(t) \\ 0 \\ 0 \end{bmatrix}}_{\text{small amplitude}}. \tag{12}$$

With this in mind, following [26], when holding $\mu$ constant suppose that (11) has a family of limit cycles $x_\mu^\gamma$ that emerge when $\mu = \begin{bmatrix} \xi & [\mathrm{Na}]_\mathrm{o} & [\mathrm{K}]_\mathrm{i} \end{bmatrix}$ for any $[\mathrm{Na}]_\mathrm{o} \in A_1 \subset \mathbb{R}$, $[\mathrm{K}]_\mathrm{i} \in A_2 \subset \mathbb{R}$ and for a specific choice of $\xi \in \mathbb{R}$. Appropriately defining an extended phase $\theta(x, [\mathrm{Na}]_\mathrm{o}, [\mathrm{K}]_\mathrm{i})$ as described in section 2.2, the associated dynamics follow

$$\begin{aligned} \dot{\theta} &= \omega([\mathrm{Na}]_\mathrm{o}, [\mathrm{K}]_\mathrm{i}) + Z(\theta, [\mathrm{Na}]_\mathrm{o}, [\mathrm{K}]_\mathrm{i})(I_\mathrm{ext}(t) - \xi)) \\ &\quad + D_\mathrm{Na}(\theta, [\mathrm{Na}]_\mathrm{o}, [\mathrm{K}]_\mathrm{i})[\dot{\mathrm{Na}}]_o + D_\mathrm{K}(\theta, [\mathrm{Na}]_\mathrm{o}, [\mathrm{K}]_\mathrm{i})[\dot{\mathrm{K}}]_i, \end{aligned} \tag{13}$$

where

$$\begin{aligned} Z(\theta, [\mathrm{Na}]_\mathrm{o}, [\mathrm{K}]_\mathrm{i}) &= \frac{\partial \theta}{\partial V}, \\ D_\mathrm{Na}(\theta, [\mathrm{Na}]_\mathrm{o}, [\mathrm{K}]_\mathrm{i}) &= -\left(\frac{\partial x^\gamma}{\partial [\mathrm{Na}]_\mathrm{o}}\right)^T Z(\theta, [\mathrm{Na}]_\mathrm{o}, [\mathrm{K}]_\mathrm{i}), \\ D_\mathrm{K}(\theta, [\mathrm{Na}]_\mathrm{o}, [\mathrm{K}]_\mathrm{i}) &= -\left(\frac{\partial x^\gamma}{\partial [\mathrm{K}]_\mathrm{i}}\right)^T Z(\theta, [\mathrm{Na}]_\mathrm{o}, [\mathrm{K}]_\mathrm{i}), \\ x(t) &\approx x_\mu^\gamma(\theta, [\mathrm{Na}]_\mathrm{o}, [\mathrm{K}]_\mathrm{i}). \end{aligned} \tag{14}$$

Above, all partial derivatives are evaluated at $x_\mu^\gamma(\theta, [\mathrm{Na}]_\mathrm{o}, [\mathrm{K}]_\mathrm{i})$. Note that since $\xi$ is constant, for notational convenience the terms from (13) and (14) are not explicitly written as functions of $\xi$. Considering the form of (13), knowledge of both $[\dot{\mathrm{Na}}]_o$ and $[\dot{\mathrm{K}}]_i$ is necessary; these terms can be computed with a copy of the slow variable dynamics evaluated according to the approximation $x(t) \approx x_\mu^\gamma(\theta, [\mathrm{Na}]_\mathrm{o}, [\mathrm{K}]_\mathrm{i})$. Ultimately, the 6 parameter model (A1) can be reduced to a system of 3 variables: one describing the phase with dynamics that follow (13), and two variables that describe the slow variable dynamics. This approach is applied to the model from (A1) using $\xi = 0.5$ so that the fast equations have a periodic orbit when $[\mathrm{K}]_\mathrm{i} \in [6.5, 12.8]$ mM and $[\mathrm{Na}]_\mathrm{o} \in [12, 20]$ mM. In (14), the phase of all $x_\mu^\gamma(\theta, [\mathrm{Na}]_\mathrm{o}, [\mathrm{K}]_\mathrm{i})$ is aligned so that $\theta = 0$

corresponds to the maximum value of $V$ on the periodic orbit (i.e., the timing of an action potential). The extended phase reduction method is compared to two other strategies. For the first, the phase reduction as described in section 3.1 is applied using the periodic orbit that results when $(\mathrm{[Na]_o}, \mathrm{[K]_i}) = (18, 7)$ mM. For the second strategy, the approach investigated in [44] is considered, whereby the entire $T_B$-periodic bursting cycle of (A1), $x^{\gamma}_{\text{burst}}(\theta)$, that results when taking $I_{\text{ext}}(t) = 0$ is considered as the periodic orbit (consisting of 37 action potentials followed by a period of quiescence). The phase reduction is applied relative to this periodic orbit yielding an equation of the form

$$\dot{\theta}_B = \omega_B + Z_B(\theta_B) I_{\text{ext}}(t), \tag{15}$$

where $\omega_B = 2\pi/T_B$. Note that for the second reduction, $\theta_B$ corresponds to the timing of the overall bursting cycle and not a timing of a single action potential.

Results comparing these reduced order models in response to pulses of length 400 ms are shown in Figure 3. Panels A, B, C, and D show voltage traces from the 3-dimensional extended phase reduction (13), the full order model (A1), the 1-dimensional phase reduction of the form (10), and the 1-dimensional bursting phase reduction of the form (15), respectively. For each of the reduced order models, the voltage is inferred as a function of phase on the appropriate periodic orbit. Specifically, the voltage is inferred from $x^{\gamma}_{\mu}(\theta)$ with $\mu = [0.5, \mathrm{[Na]_o}(t), \mathrm{[K]_i}(t)]$ for the 3-dimensional extended phase reduction, from $x^{\gamma}_{\mu}(\theta)$ with $\mu = [0.5, 18, 7]$ for the 1-dimensional phase reduction, and from $x^{\gamma}_{\text{burst}}(\theta)$ for the 1-dimensional bursting phase reduction. Panel E shows the applied transmembrane current. Here, the extended phase reduction is nearly perfect in its representation of the full order dynamics. While the single spike phase reduced model does yield spikes in response to the applied input, the spike frequency is not accurate and spikes do not persist after the input is removed. The burst cycle phase reduced model does give a bursting profile that is similar to the full order model, but the timing of the bursts is not accurate. Panel F shows the phase of oscillation plotted as a function of time for the extended, full order, and single spike phase reduced models. For the full order model, the phase is inferred by incrementing the phase by $2\pi$ at every action potential and linearly interpolating at all intermediate times. The threshold voltage for determining when an action potential occurs must be larger than the voltage reached during any afterdepolarizations at the end of the bursting cycle [39], [32]. Note that the phase, $\theta_B$, of the burst cycle phase reduction is not comparable phase, $\theta$, of the extended single spike phase models and is not shown here. Panels G and H give additional information about the profiles of the ion concentrations for each model. Recall that for the single spike phase model, the ion concentrations are constant by assumption.

While Figure 3 only gives the response to pulse inputs, it is representative of the general accuracy of each reduced order model. The extended phase reduction gives a good approximation of the overall dynamical system, but must explicitly account for the dynamics of the slow variables yielding a 3-dimensional model. By contrast, both phase reduced models require only a single variable but are only capable of capturing the dynamics local to a given limit cycle; neither of these models provide particularly accurate representations of the full model dynamics. For the single spike phase reduction, different constant values of $\mathrm{[Na]_o}$ and $\mathrm{[K]_i}$ yield models with different qualities. For instance, choosing values to the right of the line of SNIC bifurcations from panel D of Figure 1 yields models that are in a tonically firing regime in the absence of input. No matter how $\mathrm{[Na]_o}$ and $\mathrm{[K]_i}$ are chosen, the overall

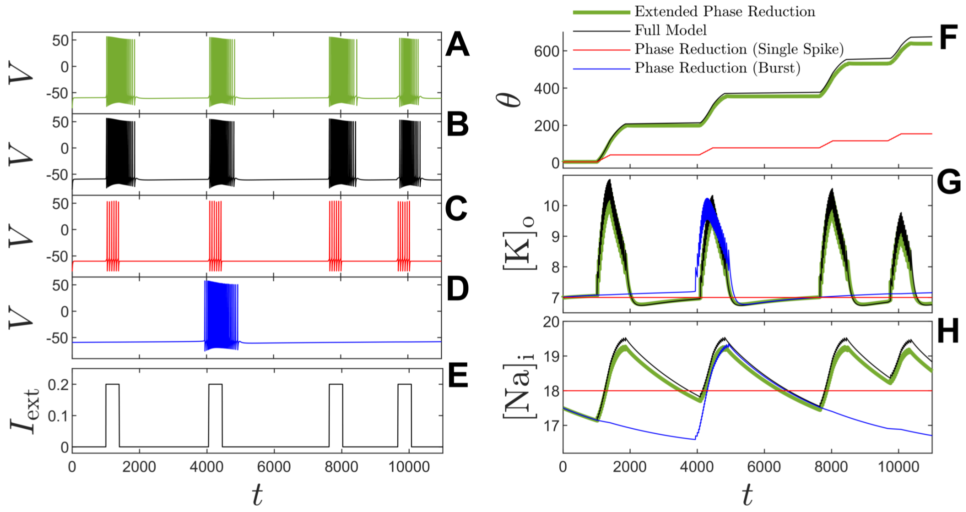

**Figure 3.** *Panels A–D show the voltage traces of three reduced order models (green, red, and blue lines) compared to the full order model (black line) in response to the series of transmembrane current impulses in panel E. Panel F shows the phase as a function of time for the full model, extended phase reduction model, and the single spike phase reduction (with each additional* $2\pi$ *in phase corresponding to an additional spike). Panels G and H show the slow variable ion concentration dynamics for each model as a function of time.*

dynamics of the single spike phase reduction do not provide a good representation of the full model dynamics. While the burst cycle phase reduction does demonstrate bursting mediated by the slow variable dynamics, it is the least accurate in terms of capturing the timing of the transition between bursting and quiescence. These results are consistent with those from [44] and [30], demonstrating considerable phase sensitivity in models of the form (15), precluding their practical use as a tool for understanding the behavior of perturbed bursters. As a final note, the results from Figure 3 illustrate an error in the total number of spikes that slowly accumulate over time. This is directly related to the fact that the input $\mu$ is comprised of both weak input and slowly varying input in the results from Figure 3 (instead of just the weak input considered in the results from Figure 2). The slowly varying input provides an additional source of error that ultimately results in a small discrepancy in the total spike count. Nonetheless, the timing of the onset and offset of bursting over time remains accurate.

## 4. Reduced order modeling for subHopf/fold cycle (elliptic) bursters.

SubHopf/fold cycle bursting (i.e., elliptic bursting) is characterized by the loss of resting stability through a subcritical Hopf bifurcation and a subsequent termination of spiking through a fold limit cycle bifurcation [22], [12]. Such bursters have a region of bistability between the resting and spiking states and often exhibit pronounced subthreshold oscillations near the critical point of the Hopf bifurcation. The Hodgkin–Huxley model [16] given in Appendix B produces elliptic bursting taking $I_{\text{ext}}$ as the bifurcation parameter (the case where bursting is mediated by a slow variable will also be considered in section 4.4). Black lines in panels A and B of Figure 4 show a bifurcation diagram, with a subcritical Hopf bifurcation occurring at $I_{\text{ext}} = 9.78\mu\text{A/cm}^2$. In panel A, example trajectories are plotted for constant values of $I_{\text{ext}}$. For $I_{\text{ext}}$ greater than the critical value, these trajectories are taken to be the resulting limit cycle. For $I_{\text{ext}}$ less than the

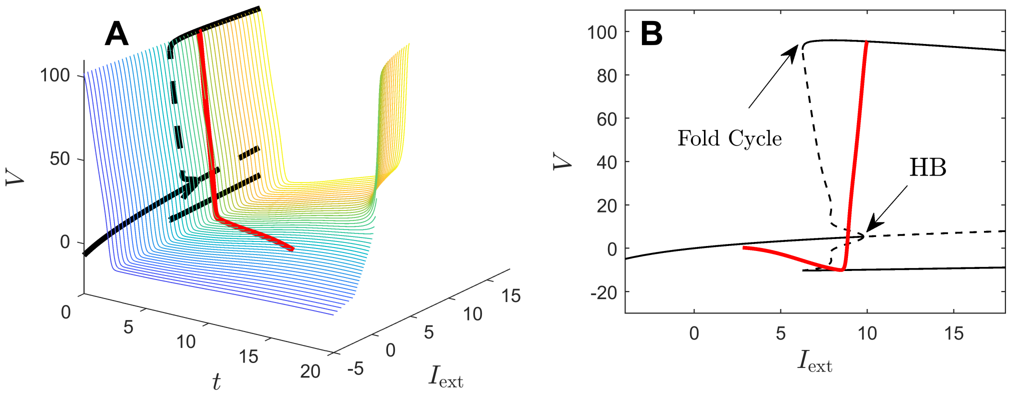

**Figure 4.** *Treating $I_{\mathrm{ext}}$ as a bifurcation parameter, black lines give the bifurcation diagram associated with the Hodgkin–Huxley model from* (B1) *as shown in panels A and B. This model has a subcritical Hopf bifurcation occurring at $I_{\mathrm{ext}} = 9.78\mu\mathrm{A/cm}^2$. Solid lines (resp., dashed) lines correspond to stable (resp., unstable) fixed points or periodic orbits. In each panel, the red line shows the voltage during a simulation for which $I_{\mathrm{ext}}(t) = 10-0.6t\,\mu\mathrm{A/cm}^2$. In this simulation, the system transitions between a periodically spiking and quiescent regime. In panel A, a collection of reference trajectories are plotted with different colors corresponding to a constant value of $I_{\mathrm{ext}}$. Section* 4 *describes a strategy to capture the behavior of a subHopf/fold cycle burster relative to a set of reference trajectories such as those shown in panel A.*

critical value, these trajectories are nonperiodic. The red line represents a simulation of the Hodgkin–Huxley model equations (B1) for which $I_{\mathrm{ext}}(t) = 10-0.6t$. Panel B is a projection of panel A into the $I_{\mathrm{ext}} - V$ plane. Even though the bifurcation parameter traverses through its critical value, the red line stays close to the reference trajectories. In this section, the proposed model order reduction represents the behavior of a subHopf/fold cycle burster relative to a set of reference trajectories such as those shown in panel A of Figure 4.

**4.1. Mathematical approach for reduction of subHopf/fold cycle bursters.** Consider a general dynamical system

$$\dot{x} = F(x,u), \tag{16}$$

where $x \in \mathbb{R}^N$ is the state, and $u \in \mathbb{R}$ is an input. Suppose that the system (16) has a Hopf bifurcation at $u = u_H$. In neuroscientific applications, a subcritical Hopf bifurcation typically leads to spiking, but the following strategy could also be applied for a supercritical Hopf bifurcation. The goal here is to represent the behavior of (16) relative to a collection of reference trajectories. Towards achieving this goal, consider a set of reference trajectories $x_{\mathrm{ref}}(\theta,p)$ that are solutions to the ordinary differential equation

$$\begin{aligned} \dot{x}_{\mathrm{ref}} &= F(x_{\mathrm{ref}},p), \\ x_{\mathrm{ref}}(0,p) &= \nu(p), \end{aligned} \tag{17}$$

where $p$ is held constant on the interval $t = [0,T(p)]$. Above, $\theta \in [0,2\pi]$ is a time-like variable where $\theta = 2\pi t/T(p)$ along solutions of (17). This set of trajectories will be used to define a reference state $x_{\mathrm{ref}}(\theta,p)$ where $p$ and $\theta$ are reduced order coordinates that will be used to characterize the dynamics of the full order system (16). The key here is to determine how $p$ and $\theta$ should change in time to accomplish this task. With this in mind, suppose that

$$x(t) = x_{\text{ref}}(\theta(t), p(t)) + \Delta x(t), \tag{18}$$

where $||\Delta x|| = O(\epsilon)$. In order for $x_{\text{ref}}(t)$ to be a good approximation of $x(t)$, $\theta(t)$ and $p(t)$ must be chosen carefully so that $\Delta x(t)$ remains an order $\epsilon$ term. To this end, Taylor expansion of (16) yields

$$\begin{aligned}\dot{x} &= F(x_{\text{ref}}(\theta, p) + \Delta x, u)\\ &= F(x_{\text{ref}}(\theta, p), p) + F_u(u - p) + F_x \Delta x + O(||\Delta x||^2) + O(||u - p||^2).\end{aligned} \tag{19}$$

Above, $F_x = \frac{\partial F}{\partial x}$, $F_u = \frac{\partial F}{\partial u}$, all partial derivatives are evaluated at $x = x_{\text{ref}}(\theta, p)$, and $u = p$. Next, direct differentiation of $x_{\text{ref}}(\theta, p)$ yields

$$\dot{x}_{\text{ref}} = \frac{\partial x_{\text{ref}}}{\partial \theta}\dot{\theta} + \frac{\partial x_{\text{ref}}}{\partial p}\dot{p}. \tag{20}$$

From (18), $\Delta \dot{x} = \dot{x} - \dot{x}_{\text{ref}}$. Substituting the results from (19) and (20) yields

$$\Delta \dot{x} = F_x \Delta x + r(\theta, p, \dot{\theta}, \dot{p}, u - p) + O(||\Delta x||^2) + O(||u - p||^2), \tag{21}$$

where

$$r(\theta, p, \dot{\theta}, \dot{p}, u - p) = F(x_{\text{ref}}(\theta, p), p) + F_u(u - p) - \frac{\partial x_{\text{ref}}}{\partial \theta}\dot{\theta} - \frac{\partial x_{\text{ref}}}{\partial p}\dot{p}. \tag{22}$$

Recall that the goal is to choose $\dot{\theta}$ and $\dot{p}$ appropriately to keep $\Delta x$ small so that $x_{\text{ref}}(t)$ is a good approximation of the full order dynamics. To gain insight on how these terms can be chosen, first suppose that both $||\Delta x||$ and $||u-p||$ from (21) are order $\epsilon$ terms. Let $(\lambda_j, v_j, w_j)$ be an eigenvalue, right eigenvector, left eigenvector triple of $F_x$ with the normalization $||v_j||_2 = w_j^T v_j = 1$. Note that $F_x$ is a function of $x(t)$ so that these eigenvalue-eigenvector pairs are all time-varying. It will be assumed that all eigenvalues of $F_x$ are simple, i.e., with algebraic multiplicity of 1. Using the coordinate transformation $y_i = w_i^T \Delta x$, one can write

$$\begin{aligned}\dot{y}_i &= \dot{w}_i^T \Delta x + w_i^T \dot{x}\\ &= \dot{w}_i^T \Delta x + w_i^T (F_x \Delta x + r)\\ &= \dot{w}_i^T \Delta x + \lambda_i y_i + w_i^T r.\end{aligned} \tag{23}$$

Above, the second line is obtained by substituting (21) and truncating the order $\epsilon^2$ terms. As shown in Appendix D, if $\lambda_i = O(1/\epsilon)$ at all times, i.e., if the decay in that direction is rapid, then $|y_i| = O(\epsilon)$. Alternatively, if $\lambda_i = O(1)$, then provided $w_i(t)^T r(t) = O(\epsilon)$ uniformly in time, $y_i(t) = O(\epsilon)$ on timescales $t \sim 1/\log(\epsilon)$. With this in mind, ideally it would be possible to find $\dot{\theta}$ and $\dot{p}$ such that $r = 0$ so that

$$0 = F(x_{\text{ref}}(\theta, p), p) + F_u(u - p) - \frac{\partial x_{\text{ref}}}{\partial \theta}\dot{\theta} - \frac{\partial x_{\text{ref}}}{\partial p}\dot{p}. \tag{24}$$

In general, however, one must settle for a least-squares minimizer. To this end, first notice that $F(x_{\text{ref}}(\theta, p), p) = \frac{\partial x_{\text{ref}}}{\partial \theta}\frac{2\pi}{T(p)}$. As such, letting $\tilde{\theta} = \theta - 2\pi t/T(p)$, one can rewrite (24) as

$$0 = F_u(u-p) - \frac{\partial x_{\text{ref}}}{\partial \theta}\dot{\dot{\theta}} - \frac{\partial x_{\text{ref}}}{\partial p}\dot{p}. \tag{25}$$

The following update rule for $\dot{\dot{\theta}}$ and $\dot{p}$ is then considered:

$$\begin{aligned}\begin{bmatrix}\dot{p}\\ \dot{\dot{\theta}}\end{bmatrix} &= \left(\exp(\alpha \text{Re}(\Lambda))W\begin{bmatrix}\frac{\partial x_{\text{ref}}}{\partial p} & \frac{\partial x_{\text{ref}}}{\partial \theta}\end{bmatrix}\right)^{\dagger}\left[\exp(\alpha \text{Re}(\Lambda))WF_u\right](u-p)\\ &= \begin{bmatrix}I(\theta,p)\\ Z(\theta,p)\end{bmatrix}(u-p),\end{aligned} \tag{26}$$

where, in the first line, $W \in \mathbb{C}^{N\times N}$ with left eigenvectors $w_i^T$ comprising its rows, $\Lambda$ is a diagonal matrix of corresponding eigenvalues, $\alpha$ is a positive constant, and $^\dagger$ denotes the pseudoinverse. In second line the terms $Z(\theta,p)$ and $I(\theta,p)$ are defined appropriately by noting that all the relevant terms in the first line are functions of both $\theta$ and $p$. Intuitively, (26) chooses $\dot{\theta}$ and $\dot{p}$ in order to minimize $r(\theta,p,\dot{\theta},\dot{p},u-p)$. The additional terms $\exp(\alpha\text{Re}(\Lambda))W$ are chosen to prioritize directions that are decaying less rapidly. Working in the coordinates $\theta$ and $p$, the reduced order dynamics become

$$\begin{aligned}\dot{\theta} &= \omega(p) + Z(\theta,p)(u-p),\\ \dot{p} &= I(\theta,p)(u-p),\end{aligned} \tag{27}$$

where $\omega(p) = 2\pi/T(p)$.

**4.2. Reduced order modeling of the Hodgkin–Huxley model.** The proposed reduction strategy will be illustrated for the Hodgkin–Huxley model [16] with equations and parameters given in Appendix B. To implement the reduction, $u$ from (16) is taken to be the baseline current, $I_{\text{ext}}$. Considering the bifurcation diagram from panel B of Figure 4, letting $I_H$ denote the external current for which the Hopf bifurcation occurs, for $I_{\text{ext}} > I_H$, $x_{\text{ref}}(\theta,p)$ will be taken to be the resulting periodic orbit. For $x_{\text{ref}}(\theta,p)$ for which $p < I_H$, the initial conditions for the reference trajectories are chosen so that $\frac{\partial x_{\text{ref}}}{\partial p}$ is continuous. Likewise, the time scaling on $x_{\text{ref}}(\theta,p)$ for $p < I_H$ is taken to be $T(p) = T(u_H) + (p-u_H)T'(u_H)$, where $'$ is the derivative with respect to $p$ so that $T(p)$ is continuously differentiable. This strategy gives the resulting periodic orbits, shown as a function of $\theta$ in panel A of Figure 5. $Z(\theta,p)$ and $I(\theta,p)$ are computed as defined in (26) taking $\alpha = 0.4$. In order to avoid infinitely large values of $I$ and $Z$, when taking the pseudoinverse in this computation, all singular values smaller than 0.1 are truncated. Panels B and C show both $Z(\theta,p)$ and $I(\theta,p)$ associated with the $p=1$ reference trajectory. Note that this trajectory approaches a fixed point for the latter values of $\theta$. These curves are consistent with results discussed in section 4.3.2 after (45); as trajectories approach the stable fixed point associated with a Hopf bifurcation, $Z(\theta)$ and $I(\theta)$ resemble the cosecant and cotangent functions, respectively. Panels D and E give the same information for the $p = 15\mu\text{A/cm}^2$ reference trajectory, which is a periodic orbit. Additional information about the local decay rates along these trajectories is given in Figure 6. Panels A and C show the real components of the eigenvalues of the Jacobian as a function of $\theta$ for the $p = 1\ \mu\text{A/cm}^2$ and $p = 15\ \mu\text{A/cm}^2$ trajectories, respectively. Panels B and D show the residual defined according to (22) in the associated eigenvector basis. When computing $Z(\theta,p)$ and $I(\theta,p)$ as defined in

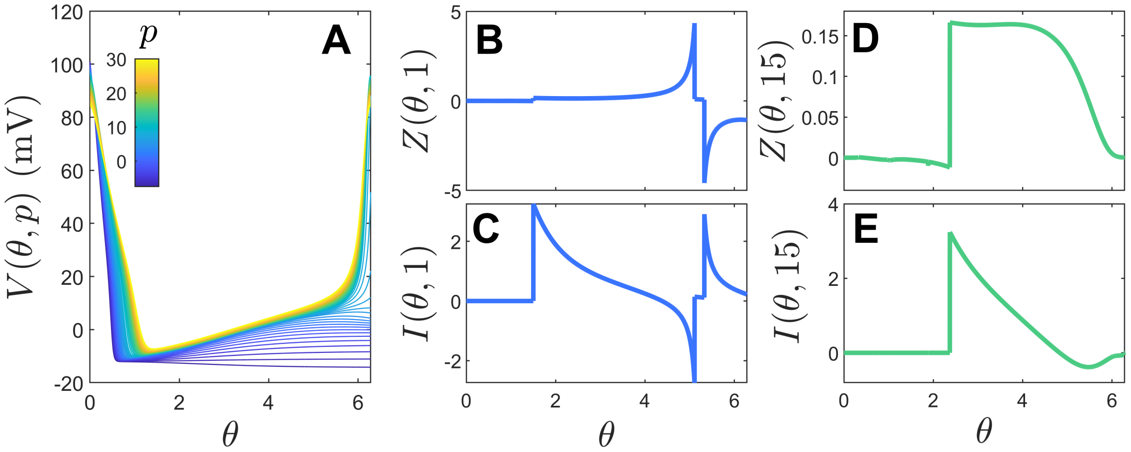

**Figure 5.** *Trajectories $x_{\mathrm{ref}}(\theta,p)$ used in the reduced order representation of the Hodgkin–Huxley model are shown in panel A for $p \in [-8,30]$ $\mu$A/cm$^2$. Panels B and C (resp., D and E) show the terms $Z(\theta)$ and $I(\theta)$ computed according to (26) for the $p=1$ $\mu$A/cm$^2$ (resp., $p=15$ $\mu$A/cm$^2$) trajectory.*

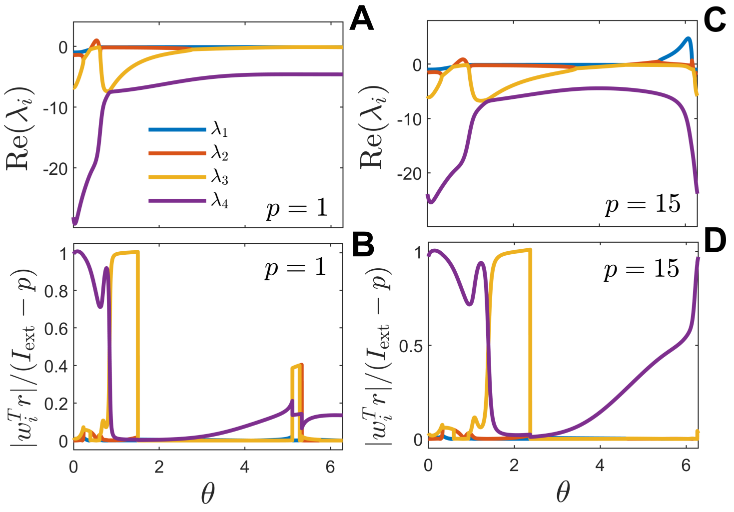

**Figure 6.** *Panels A and C show the real component of the eigenvalues of the Jacobian as a function of $\theta$ for the $p=1$ and $p=15$ $\mu$A/cm$^2$ reference trajectories, respectively. Panels B and D give the corresponding residual defined according to (22) in a basis of eigenvectors when choosing $\dot{\theta}$ and $\dot{p}$ as mandated by (27). For* $\mathrm{Re}(\lambda_i)$ *that is negative and large in magnitude, the associated residual can be large because the decay is fast in that direction. Otherwise the residual must be small to limit the magnitude of the errors in the resulting reduced order model. The functions $Z(\theta,p)$ and $I(\theta,p)$ as defined in E(26) are designed to accommodate this requirement.*

(26), minimization of the residual in a given eigendirection is balanced against the decay rate, as gauged by the real component of the associated eigenvalue.

Figure 7 illustrates the accuracy of the reduced order modeling strategy in comparison with a standard phase reduction approach [12, 22] discussed in section 2. To implement the standard phase reduction, the periodic orbit $x^{\gamma}(\theta,12) = x_{\mathrm{ref}}(\theta,12)$ is used to define

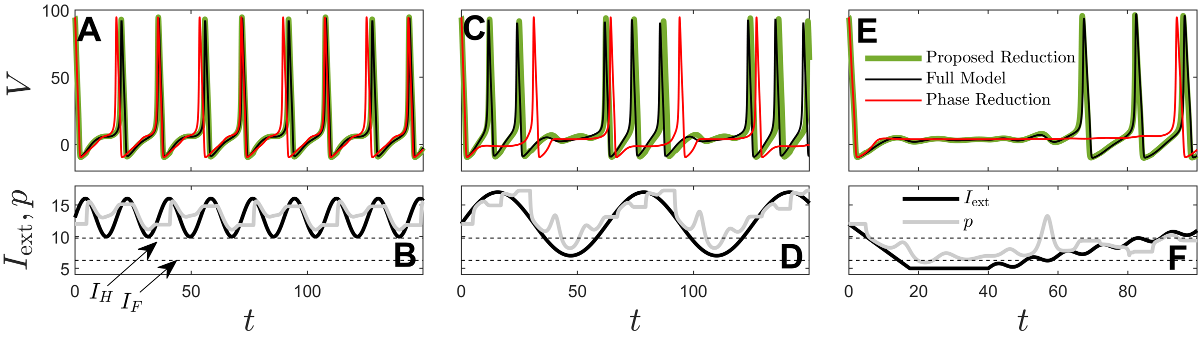

**Figure 7.** *The three inputs shown as black lines in panels B, D, and F are applied to the full order Hodgkin–Huxley model from* (B1)*, the proposed reduced order model from* (27)*, and the standard phase reduction of the form* (4)*. Horizontal lines denoting the value at which the Hopf bifurcation and fold cycle bifurcation occur* ($I_H$ *and* $I_F$*, respectively) are provided for reference. Corresponding traces of the transmembrane voltage are shown in panels A, C, and E. Traces of* $p$ *for simulations of the proposed strategy are shown in grey in panels B, D, and F. In general, standard phase reduction provides a reasonably accurate approximation of the model dynamics when the input stays in the tonically firing regime. However, for transitions between firing and quiescence, only the proposed reduction strategy accurately captures the behavior.*

isochrons (3); when writing the Hodgkin–Huxley equations from (B1) in the same form as (2), $I_{\text{ext}}(\mu) = 12 + \mu$. The terms of the phase response curve are computed numerically via the adjoint method [31]. Panel A of Figure 7 shows both the phase reduction and the proposed reduction strategy in response to the input $I_{\text{ext}}(t) = 13 + 3\sin(0.35t)$ $\mu\text{A}/\text{cm}^2$ shown in panel B. This input is chosen purposely so $|\mu|$ remains relatively small when implementing the phase reduction (4). In this case both the phase reduction and proposed reduced order model provide a good approximation of the full order dynamics with both models correctly predicting entrainment to the external input. Panel C shows the same results for an input $I_{\text{ext}}(t) = 12 + 5\sin(0.1t)$ $\mu\text{A}/\text{cm}^2$ from panel D which briefly drops below $I_H = 9.78\mu\text{A}/\text{cm}^2$ (the value at which the Hopf bifurcation occurs). In response to this input, spiking temporarily stops when $I_{\text{ext}}(t)$ nears its lowest point. In this case, the phase reduction does not accurately capture the transition from spiking to quiescence, while the proposed model does; conversely the proposed model provides a near perfect representation of the model. A third stimulus shown in panel F gradually decreases $I_{\text{ext}}(t)$ below $I_F = 6.26\mu\text{A}/\text{cm}^2$ (the value at which the fold cycle bifurcation occurs) in order to transition from firing to quiescence. For $t > 40$, $I_{\text{ext}}(t) = 5 + 0.1(t - 40) + 0.5\sin(0.63t)$. The resonance with the added sine wave input yields an action potential before the crossing of $I_H$, which is accurately reflected by the proposed reduced order model. Once again, the phase reduced model fails to replicate the full order dynamics for this input.

### 4.3. Coexistence of stable attractors in the reduced order model characterizing sub-Hopf/fold cycle bursters.

Results from Figure 7 illustrate the ability of the reduced order model (27) to replicate both periodic firing and quiescence observed in the full order model (16). The analysis below illustrates that with appropriate technical constraints on the full order model and with a careful choice of reference trajectories, $x_{\text{ref}}(\theta)$, stable periodic orbits and fixed points that capture the transitions between periodic firing and quiescence are guaranteed to exist in the reduced order model (27).

**4.3.1. Existence and stability of periodic orbits of the reduced order equations.** Suppose that $x_{\text{ref}}(\theta,p_0)$ for a constant $p_0$ is chosen as a stable periodic orbit $x^\gamma_{p_0}(\theta)$ of the dynamical system (16) with period $\omega(p_0)=2\pi/T(p_0)$. The stability of $x^\gamma_{p_0}$ can be characterized by considering the Floquet exponents $\kappa_1,\dots,\kappa_N$ associated with linearization of (16) about the periodic orbit [23]. Let $\Delta x(t)=x(t)-x^\gamma_{p_0}(\theta(t))$, where $x(t)$ evolves according to the full system of equations (16). When $||\Delta x||$ is small, using Floquet theory [23], one can write

$$\Delta x(t)=\sum_{j=1}^{N} c_j g_j(t)\exp(\kappa_j t)+O(||dx||^2), \tag{28}$$

where $g_1(t),\dots,g_N(t)$ are $T(p_0)$-periodic Floquet eigenfunctions, and the constants $c_1,\dots,c_N$ are chosen to satisfy initial conditions. The Floquet exponents will be ordered so that $\kappa_1=0$ (corresponding to translation along the periodic orbit so that $g_1(t)=\frac{\partial x_{\text{ref}}}{\partial\theta}$). Because $x^\gamma_{p_0}$ is stable, the remaining Floquet exponents $\kappa_2,\dots,\kappa_N$ have negative real component. We will assume that $\exp(\kappa_j T(p_0))=O(\epsilon)$ for $j\geq 3$ so there is at most one slowly decaying Floquet eigenfunction.

Considering the form of the reduced order equations from (27) and recalling the choice $x_{\text{ref}}(\theta,p_0)=x^\gamma_{p_0}(\theta)$, clearly this transformed system contains the periodic orbit $(\theta^\gamma(t),p^\gamma(t))=(\omega(p_0)t+\theta_0,p_0)$, where $\theta_0$ is a constant offset. Towards determining the stability of the periodic orbit of the reduced order equation (27), consider a small perturbation $\Delta\theta=\theta(t)-\theta^\gamma(t)$ and $\Delta p=p(t)-p^\gamma(t)$. Considering (27), suppose that the conditions given above (24) are satisfied (i.e., for every $\lambda_i(t)$ from $i=1,\dots,N$, either $\lambda_i(t)=O(1/\epsilon)$ for all $t$ or $w_i(t)^T r(t)=O(\epsilon)$ for all $t$). Then $x_{\text{ref}}(t)=x(t)+O(\epsilon)$ and one can write

$$\begin{aligned} x(t)&=x_{\text{ref}}(\theta^\gamma(t)+\Delta\theta,p^\gamma(t)+\Delta p)+O(\epsilon)\\ &=x_{\text{ref}}(\theta^\gamma(t),p^\gamma(t))+\frac{\partial x_{\text{ref}}}{\partial\theta}\Delta\theta(t)+\frac{\partial x_{\text{ref}}}{\partial p}\Delta p(t), \end{aligned}\tag{29}$$

where the second line results from Taylor expansion after truncating $O(\epsilon)$, $O(|\Delta\theta|^2)$, and $O(|\Delta p|^2)$ terms. Noting that $x_{\text{ref}}(\theta^\gamma(t),p^\gamma(t))=x^\gamma_{p_0}(\theta(t))$, rearranging (29) yields

$$\begin{aligned} \Delta x(t)&=\frac{\partial x_{\text{ref}}}{\partial\theta}\Delta\theta(t)+\frac{\partial x_{\text{ref}}}{\partial p}\Delta p(t)\\ &=(\Delta\theta(t)+a_1\Delta p(t))g_1(t)+a_2\Delta p(t)g_2(t)+\sum_{j=3}^{N}a_j\Delta p(t)g_j(t). \end{aligned}\tag{30}$$

Above, the second line is obtained by writing $\frac{\partial x_{\text{ref}}}{\partial\theta}$ and $\frac{\partial x_{\text{ref}}}{\partial p}$ in a basis of Floquet eigenfunctions; here, $\frac{\partial x_{\text{ref}}}{\partial\theta}=g_1(t)$ and $\frac{\partial x_{\text{ref}}}{\partial p}=\sum_{j=1}^N a_j g_j(t)$. Applying (28) to (30), recalling that $\exp(\kappa_j T(p_0))=O(\epsilon)$, one finds

$$\Delta x(T)=(\Delta\theta(0)+a_1\Delta p(0))g_1(T)+a_2\exp(\kappa_2 T)\Delta p(0)g_2(T)+O(\epsilon). \tag{31}$$

Considering (31) and evaluating (30) at $t=T$, matching the coefficients in front of $g_1(t)$ and $g_2(t)$, and dropping $O(\epsilon)$ terms, one finds

$$\begin{aligned}\begin{bmatrix}\Delta\theta(T)\\ \Delta p(T)\end{bmatrix} &= \begin{bmatrix}1 & a_1(1-\exp(\kappa_2 T))\\ 0 & \exp(\kappa_2 T)\end{bmatrix}\begin{bmatrix}\Delta\theta(0)\\ \Delta p(0)\end{bmatrix}\\ &= \Phi\begin{bmatrix}\Delta\theta(0)\\ \Delta p(0)\end{bmatrix}.\end{aligned}\tag{32}$$

Equation (32) provides a good approximation of the monodromy matrix, $\Phi$, associated with the linearization of the periodic orbit $(\theta^\gamma(t), p^\gamma(t)) = (\omega(p_0)t+\theta_0, p_0)$ of (27). Since $\mathrm{Re}(\kappa_2) < 0$, the nonunity eigenvalues of this periodic orbit are inside the unit circle and the periodic orbit is stable.

**4.3.2. Existence of fixed points of the reduced order equations.** In addition to the existence of stable periodic orbits, one can also prove the existence of stable fixed points in the reduced order model of the form (27) when the parameter $p$ is close to the Hopf bifurcation. To begin, consider a trajectory $x_{\mathrm{ref}}(\theta, p)$ for which $x_{\mathrm{ref}}(2\pi, p) - x_{\mathrm{ss}}(p) = O(\epsilon)$, where $x_{\mathrm{ss}}(p)$ is a stable fixed point of (16), i.e., for which $F(x_{\mathrm{ss}}, p) = 0$. For states close enough to the fixed point, the state is well approximated by

$$x_{\mathrm{ref}}(\theta, p) = \sum_{j=1}^{N} s_i \exp(\lambda_j \theta/\omega) v_j, \tag{33}$$

where $(\lambda_j, v_j)$ are an eigenvalue-eigenvector pair of the Jacobian, $F_x$ evaluated at $x_{\mathrm{ss}}$, $s_i$ gives the coordinate in the basis of eigenvectors, and $t = \theta/\omega$ along the trajectories $x_{\mathrm{ref}}(\theta, p)$. Also let $w_i$ be a corresponding left eigenvector with the normalization $w_i^T v_i = 1$. Along reference trajectories,

$$\frac{\partial x_{\mathrm{ref}}}{\partial \theta} = \sum_{j=1}^{N} \frac{s_i \lambda_i}{\omega} \exp(\lambda_i \theta/\omega) v_j. \tag{34}$$

Considering a nearby trajectory $x_{\mathrm{ref}}(\theta, p + \Delta p)$ with $\Delta p = O(\epsilon)$, as illustrated in Figure 8, provided $\theta/\omega$ is large enough,

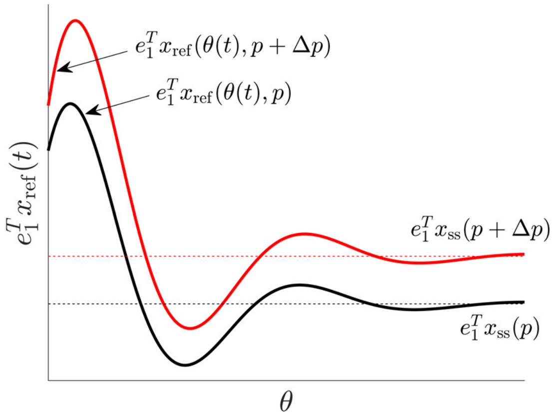

**Figure 8.** *For $p$ close to a Hopf bifurcation, if a reference trajectory $x_{\mathrm{ref}}(\theta, p)$ approaches a stable fixed point $x_{\mathrm{ss}}(p)$ of the underlying system $\dot{x} = F(x, p)$, the system can be considered in terms of its linearization about $x_{\mathrm{ss}}$. Note above that $e_1^T = [1 \ \ldots \ 0]$.*

$$x_{\text{ref}}(\theta, p+\Delta p) - x_{\text{ref}}(\theta, p) = x_{\text{ss}}(p+\Delta p) - x_{\text{ss}}(p) + O(\epsilon^2). \tag{35}$$

Towards simplifying (35) further, note that at each fixed point, $0 = F(x_{\text{ss}}(p+\Delta p), p+\Delta p) = F(x_{\text{ss}}(p), p)$. With this in mind, $0 = F(x_{\text{ss}}(p) + (x_{\text{ss}}(p+\Delta p) - x_{\text{ss}}(p), p+\Delta p)$, which can subsequently be Taylor expanded and rearranged to yield

$$F_x(x_{\text{ss}}(p+\Delta p) - x_{\text{ss}}(p)) = -\frac{\partial F}{\partial u}\Delta p + O(\epsilon^2). \tag{36}$$

Through diagonalization of $F_x$ and subsequent manipulation of (36), one can obtain

$$x_{\text{ss}}(p+\Delta p) - x_{\text{ss}}(p) = -\Delta p \sum_{j=1}^{N} \frac{w_j^T \frac{\partial F}{\partial u}}{\lambda_j} v_j + O(\epsilon^2). \tag{37}$$

Considering (37), for $\theta$ large enough, along reference trajectories,

$$\frac{\partial x_{\text{ref}}}{\partial p} = -\sum_{j=1}^{N} \frac{w_j^T \frac{\partial F}{\partial u}}{\lambda_j} v_j. \tag{38}$$

Next, let $\lambda_{1,2}$ be the complex-conjugate eigenvalues responsible for the Hopf bifurcation ordered so that $\text{Im}(\lambda_1) > 0$. Additionally, let the associated eigenvectors be scaled so that $v_1 = v_2^*$, where $^*$ denotes the complex-conjugate. Assume that $p \approx u_H$ so that the system is close to the Hopf bifurcation and $\text{Re}(\lambda_1)$ is small. Considering the definition of $Z$ and $I$ from (26), with $\alpha$ large enough one finds

$$\begin{aligned} \begin{bmatrix} Z(\theta,p) \\ I(\theta,p) \end{bmatrix} &= \left( \exp(\alpha \text{Re}(\Lambda)) W \begin{bmatrix} \frac{\partial x_{\text{ref}}}{\partial p} & \frac{\partial x_{\text{ref}}}{\partial \theta} \end{bmatrix} \right)^{\dagger} \left[ \exp(\alpha \text{Re}(\Lambda)) W \frac{\partial F}{\partial u} \right] \\ &= \begin{bmatrix} A \\ \epsilon C_1 \end{bmatrix}^{\dagger} \begin{bmatrix} B \\ \epsilon C_2 \end{bmatrix}, \end{aligned} \tag{39}$$

where

$$\begin{aligned} A &= \begin{bmatrix} \exp(\alpha \text{Re}(\lambda_1)) & 0 \\ 0 & \exp(\alpha \text{Re}(\lambda_2)) \end{bmatrix} \begin{bmatrix} w_1 & w_2 \end{bmatrix}^T \begin{bmatrix} \frac{\partial x_{\text{ref}}}{\partial p} & \frac{\partial x_{\text{ref}}}{\partial \theta} \end{bmatrix} \in \mathbb{C}^{2\times 2}, \\ B &= \begin{bmatrix} \exp(\alpha \text{Re}(\lambda_1)) & 0 \\ 0 & \exp(\alpha \text{Re}(\lambda_2)) \end{bmatrix} \begin{bmatrix} w_1 & w_2 \end{bmatrix}^T \frac{\partial F}{\partial u} \in \mathbb{C}^{2\times 1}, \end{aligned} \tag{40}$$

and $C_1$ and $C_2$ are both in $\mathbb{C}^{N-2\times 2}$ containing order $\epsilon$ terms because $\alpha\text{Re}(\lambda_i) = O(\epsilon)$ for $i > 2$ (i.e., for the faster decaying terms). Further manipulating $A$ from (40), substituting (34) and (38) for $\frac{\partial x_{\text{ref}}}{\partial \theta}$ and $\frac{\partial x_{\text{ref}}}{\partial p}$ yields

$$\begin{aligned} A &= \begin{bmatrix} \exp(\alpha \text{Re}(\lambda_1)) & 0 \\ 0 & \exp(\alpha \text{Re}(\lambda_2)) \end{bmatrix} \begin{bmatrix} -w_1^T \frac{\partial F}{\partial u}/\lambda_1 & \frac{T(p)}{2\pi} s_1 \lambda_1 \exp(\lambda_1 \theta/\omega) \\ -w_2^T \frac{\partial F}{\partial u}/\lambda_2 & \frac{T(p)}{2\pi} s_2 \lambda_2 \exp(\lambda_2 \theta/\omega) \end{bmatrix} \\ &= \begin{bmatrix} \exp(\alpha \text{Re}(\lambda_1)) & 0 \\ 0 & \exp(\alpha \text{Re}(\lambda_2)) \end{bmatrix} \begin{bmatrix} \mu & \zeta \exp(\lambda_1 \theta/\omega) \\ \mu^* & \zeta^* \exp(\lambda_1^* \theta/\omega) \end{bmatrix}, \end{aligned} \tag{41}$$

where $\mu = -w_1^T \frac{\partial F}{\partial u} / \lambda_1$ and $\zeta = s_1 \lambda_1 \frac{T(p)}{2\pi}$. Provided $A$ is full rank,

$$\begin{aligned}
\begin{bmatrix} A \\ \epsilon C_1 \end{bmatrix}^{\dagger} &= \left( \begin{bmatrix} A^H & \epsilon C_1^H \end{bmatrix} \begin{bmatrix} A \\ \epsilon C_1 \end{bmatrix} \right)^{-1} \begin{bmatrix} A^H & \epsilon C_1^H \end{bmatrix} \\
&= \left( A^H A + \epsilon^2 C_1^H C_1 \right)^{-1} \begin{bmatrix} A^H & \epsilon C_1^H \end{bmatrix} \\
&= ((A^H A)^{-1} + O(\epsilon^2)) \begin{bmatrix} A^H & \epsilon C_1^H \end{bmatrix} \\
&= \begin{bmatrix} A^{\dagger} & 0 \end{bmatrix} + O(\epsilon) \\
&= \begin{bmatrix} A^{-1} & 0 \end{bmatrix} + O(\epsilon). \qquad (42)
\end{aligned}$$

Above, $^H$ denotes the Hermitian transpose, line 3 is obtained noting that $\epsilon^2 B^H B$ is a small perturbation, the zero in line 4 is an appropriately sized matrix of zeros, and line 5 follows because $A$ is full rank. Substituting (42) into (39) and neglecting $O(\epsilon)$ terms yields

$$\begin{aligned}
\begin{bmatrix} Z(\theta,p) \\ I(\theta,p) \end{bmatrix} &= \begin{bmatrix} A^{-1} & 0 \end{bmatrix} \begin{bmatrix} B \\ 0 \end{bmatrix} \\
&= \frac{1}{\mu\zeta \exp(\lambda_1^* \theta/\omega) - \mu^* \zeta \exp(\lambda_1 \theta/\omega)} \begin{bmatrix} \zeta^* \exp(\lambda_1^* \theta/\omega) & -\zeta \exp(\lambda_1 \theta/\omega) \\ -\mu^* & \mu \end{bmatrix} \begin{bmatrix} -\mu\lambda_1 \\ -\mu^* \lambda_1^* \end{bmatrix} \\
&= \frac{-1}{\mathrm{Im}(\mu^* \zeta \exp(\lambda_1 \theta/\omega))} \begin{bmatrix} \mathrm{Im}(\mu^* \lambda_1^* \zeta \exp(\lambda_1 \theta/\omega)) \\ |\mu|^2 \mathrm{Im}(\lambda_1) \end{bmatrix} \\
&= \frac{-1}{|\mu\zeta| \exp(\mathrm{Re}(\lambda_1)\theta/\omega) \sin(\angle(\mu^*\zeta) + \mathrm{Im}(\lambda_1 \theta/\omega))} \\
&\quad \times \begin{bmatrix} |\mu\zeta\lambda_1| \exp(\mathrm{Re}(\lambda_1)\theta/\omega) \sin(\angle(\mu^*\zeta\lambda_1^*) + \mathrm{Im}(\lambda_1\theta/\omega)) \\ |\mu|^2 \mathrm{Im}(\lambda_1)) \end{bmatrix}, \qquad (43)
\end{aligned}$$

where $\angle(\cdot)$ and $|\cdot|$ denote the argument and magnitude of a given complex number. Finally, simplifying (43), one can write

$$I(\theta,p) = \frac{-|\lambda_1| \sin(\angle(\mu^*\zeta\lambda_1^*) + \mathrm{Im}(\lambda_1\theta/\omega))}{\sin(\angle(\mu^*\zeta) + \mathrm{Im}(\lambda_1\theta/\omega))}, \qquad (44)$$

$$Z(\theta,p) = \frac{-|\mu| \mathrm{Im}(\lambda_1)}{|\zeta| \exp(\mathrm{Re}(\lambda_1)\theta/\omega) \sin(\angle(\mu^*\zeta) + \mathrm{Im}(\lambda_1\theta/\omega))}. \qquad (45)$$

Noting that $\angle(\lambda_1) \approx \pi/2$, $I(\theta,p)$ is well approximated by the cotangent function while $Z(\theta,p)$ is well approximated by the cosecant which is consistent with results shown in panel C of Figure 5; note that this approximation is only valid for larger values of $\theta$. Considering the form of the reduced order equations (27) and the terms $I(\theta,p)$ and $Z(\theta,p)$ obtained in (44) and (45), respectively, when $u = \bar{u}$ is held constant, (27) has fixed points at $(\bar{\theta}, \bar{p})$ where $I(\bar{\theta}, \bar{p}) = 0$ with corresponding

$$Z(\bar{\theta}, \bar{p}) = -\frac{\omega(\bar{p})}{\bar{u} - \bar{p}}. \qquad (46)$$

### 4.3.3. Stability of fixed points of the reduced order equations.

The stability of this fixed point can be determined by examining the Jacobian of the linearization of (27),

$$J_r = \begin{bmatrix} Z_\theta(u-p) & \omega_p + Z_p(u-p) - Z \\ I_\theta(u-p) & I_p(u-p) - I \end{bmatrix}, \qquad (47)$$

where the notation $Z_p$, for instance, denotes the partial derivative taken with respect to $p$ with all partial derivatives evaluated at $\theta = \bar{\theta}$ and $p = \bar{p}$. Recalling that $I = 0$ at the fixed point, considering the numerator of (44), $\angle(\mu^* \zeta \lambda_1^*) + \text{Im}(\lambda_1 \theta/\omega) = k\pi$ for some integer value of $k$. As such the denominator of (44) is given by $\sin(\angle(\lambda_1) + k\pi)$. Recalling that the parameter set is chosen near the Hopf bifurcation so that $\angle(\lambda_1) = \pi/2$, $|\sin(\angle(\lambda_1) + k\pi)| \approx 1$ meaning that $I(\theta, p)$ and its partial derivatives are $O(1)$ terms. Recalling the assumption below (22) that $u - p$ is an order $\epsilon$ term, considering (46), $Z(\theta, p)$ and its partial derivatives are $O(1/\epsilon)$ terms. The eigenvalues of the Jacobian from (47) can be computed directly according to

$$\lambda_r = \frac{\text{Tr}(J_r) \pm \sqrt{\text{Tr}(J_r)^2 - 4\text{Det}(J_r)}}{2}, \tag{48}$$

where $\text{Tr}(J_r)$ and $\text{Det}(J_r)$ are the trace and determinant of $J_r$, respectively. Using this relation, ignoring $O(\epsilon)$, one finds

$$\lambda_r = \frac{Z_\theta(u-p) \pm \sqrt{(Z_\theta(u-p))^2 - 4ZI_\theta(u-p)}}{2}. \tag{49}$$

Recalling that at at the fixed point, $\sin(\angle(\mu^*\zeta) + \text{Im}(\lambda_1\theta/\omega)) = \sin(\angle(\lambda_1) + k\pi)$, where $k$ is an integer, straightforward differentiation of (45) and subsequent simplification using trigonometric identities yields

$$Z_\theta(\bar{\theta}, \bar{p}) = \frac{-2\text{Re}(\lambda_1) Z(\bar{\theta}, \bar{p})}{\omega}, \tag{50}$$

$$I_\theta(\bar{\theta}, \bar{p}) = \frac{-|\lambda_1|^2}{\omega}. \tag{51}$$

Substituting (50), (51), and (46) into (49) and simplifying yields

$$\lambda_r = \text{Re}(\lambda_1) \pm \text{Imag}(\lambda_1) i, \tag{52}$$

i.e., the fixed point is stable with identical eigenvalues to the slowest decaying terms of the full order model.

### 4.4. SubHopf/fold cycle bursting with slow variable dynamics.

It is relatively straightforward to explicitly include slow variable dynamics in the reduction approach from section 4.1. To do so, consider a general system

$$\begin{aligned} \dot{x} &= f(x, y, u), \\ \dot{y} &= \epsilon g(x, y), \end{aligned} \tag{53}$$

where $x \in \mathbb{R}^N$ and $y \in \mathbb{R}^k$ denote the fast and slow variables with dynamics governed by $f$ and $g$, respectively, and $u \in \mathbb{R}$ is an input. Such a system could describe, for instance, a neuron where the bursting is mediated by the slow variable dynamics that also receives an additional synaptic current from an external source. Following the approach from section 4.1, one can define a set of reference trajectories $x_{\text{ref}}(\theta, p, y_{\text{ref}})$ that are solutions to

$$\begin{aligned} \dot{x}_{\text{ref}} &= f(x_{\text{ref}}, p, y_{\text{ref}}), \\ x_{\text{ref}}(0, p, y_{\text{ref}}) &= \nu(p, y_{\text{ref}}), \end{aligned} \tag{54}$$

where both $p$ and $y_{\text{ref}}$ are held constant on the interval $t=[0,T(p)]$. Once again, $\theta\in[0,2\pi]$ is a time-like variable where $\theta=2\pi t/T(p)$ along solutions of (54). Notice that (54) is identical to (17) with the addition of the term $y_{\text{ref}}$. Using the trajectories obtained from (54) for reference, allowing $\theta$, $p$, and $y_{\text{ref}}$ to change in time and taking the total time derivative of $x_{\text{ref}}(\theta,p,y_{\text{ref}})$ yields

$$\dot{x}_{\text{ref}}=\frac{\partial x_{\text{ref}}}{\partial\theta}\dot{\theta}+\frac{\partial x_{\text{ref}}}{\partial p}\dot{p}+\frac{\partial x_{\text{ref}}}{\partial y_{\text{ref}}}\dot{y}_{\text{ref}}. \tag{55}$$

Mirroring the arguments from (17) to (21), one can define $\Delta x = x - x_{\text{ref}}(\theta,p,y_{\text{ref}})$ and $\Delta y = y - y_{\text{ref}}$. Taylor expansion of (53) relative to $x_{\text{ref}}$ and $y_{\text{ref}}$ yields

$$\begin{aligned}
\dot{x}&=f(x_{\text{ref}}(\theta,p,y_{\text{ref}}),y_{\text{ref}},p)+f_u(u-p)+f_x\Delta x+O(||\Delta x||^2)+O(||u-p||^2)+O(||\Delta y||),\\
\dot{y}&=\epsilon g(x_{\text{ref}},y_{\text{ref}})+O(\epsilon||\Delta x||)+O(\epsilon||\Delta y||),
\end{aligned}\tag{56}$$

where $f_x\equiv\frac{\partial f}{\partial x}$, $f_u\equiv\frac{\partial f}{\partial u}$, each evaluated at $x_{\text{ref}}$, $y_{\text{ref}}$, and $p$. Combining (55) and (56), one can write

$$\Delta\dot{x}=f_x\Delta x+r(\theta,p,y_{\text{ref}},\dot{\theta},\dot{p},\dot{y}_{\text{ref}},u-p)+O(||\Delta x||^2)+O(||u-p||^2)+O(||\Delta y||^2), \tag{57}$$

$$\Delta\dot{y}=\epsilon g(x_{\text{ref}},y_{\text{ref}})-\dot{y}_{\text{ref}}+O(\epsilon||\Delta x||)+O(\epsilon||\Delta y||), \tag{58}$$

where

$$\begin{aligned}
r(\theta,p,y_{\text{ref}},\dot{\theta},\dot{p},\dot{y}_{\text{ref}},u-p)&=f(x_{\text{ref}}(\theta,p,y_{\text{ref}}),y_{\text{ref}},p)+f_u(u-p)\\
&\quad-\frac{\partial x_{\text{ref}}}{\partial\theta}\dot{\theta}-\frac{\partial x_{\text{ref}}}{\partial p}\dot{p}-\frac{\partial x_{\text{ref}}}{\partial y_{\text{ref}}}\dot{y}_{\text{ref}}.
\end{aligned}\tag{59}$$

Provided $\Delta x$ and $\Delta y$ are small, $x_{\text{ref}}$ and $y_{\text{ref}}$ provide good approximations for $x$ and $y$ from the underlying system (53). Considering the $\Delta y$ dynamics from (58) first, taking

$$\dot{y}_{\text{ref}}=\epsilon g(x_{\text{ref}},y_{\text{ref}}) \tag{60}$$

eliminates all but the $O(\epsilon||\Delta x||)$ and $O(\epsilon||\Delta y||)$ terms from (58). Following the strategy from section 4.1, considering (57) the growth of $\Delta\dot{x}$ can be limited by minimizing $r(t)$ and prioritizing directions that decay less rapidly as gauged by the eigendecomposition of $f_x$. Mirroring the arguments from (21) to (26), letting $\tilde{\theta}=\pi-2\pi t/T(p)$, an update rule that accomplishes this task is

$$\begin{aligned}
\begin{bmatrix}\dot{p}\\ \dot{\tilde{\theta}}\end{bmatrix}&=\left(\exp(\alpha\text{Re}(\Lambda))W\begin{bmatrix}\frac{\partial x_{\text{ref}}}{\partial p} & \frac{\partial x_{\text{ref}}}{\partial\theta}\end{bmatrix}\right)^{\dagger}\left[\exp(\alpha\text{Re}(\Lambda))Wf_u\right](u-p)\\
&\quad-\left(\exp(\alpha\text{Re}(\Lambda))W\begin{bmatrix}\frac{\partial x_{\text{ref}}}{\partial p} & \frac{\partial x_{\text{ref}}}{\partial\theta}\end{bmatrix}\right)^{\dagger}\left[\exp(\alpha\text{Re}(\Lambda))W\frac{\partial x_{\text{ref}}}{\partial y_{\text{ref}}}\right]\dot{y}_{\text{ref}}\\
&=\begin{bmatrix}I(\theta,p,y_{\text{ref}})\\ Z(\theta,p,y_{\text{ref}})\end{bmatrix}(u-p)-\begin{bmatrix}\tilde{I}(\theta,p,y_{\text{ref}})\\ \tilde{Z}(\theta,p,y_{\text{ref}})\end{bmatrix}\dot{y}_{\text{ref}},
\end{aligned}\tag{61}$$

where in the first line (as in section 4.1) $W\in\mathbb{C}^{N\times N}$ with left eigenvectors of $f_x$ comprising its rows, $\Lambda$ is a diagonal matrix of corresponding eigenvalues, $\alpha$ is a positive constant, and $^{\dagger}$

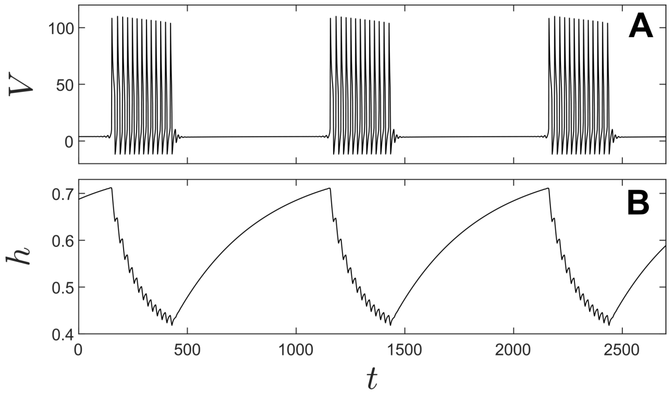

**Figure 9.** *With minor modifications described in the text, the Hodgkin–Huxley model from Appendix B displays elliptic bursting mediated by the slow variable $h$. In a representative simulation taking $I_{\text{ext}} = 0$, the transmembrane voltage and slow variable are shown in panels A and B, respectively.*

denotes the pseudoinverse. In the second line the terms $Z$, $\tilde{Z}$, $I$, and $\tilde{I}$ are defined appropriately by noting that all relevant terms in the first line are functions of $\theta$, $p$, and $y_{\text{ref}}$. Using in the coordinates $\theta$, $p$, and $y_{\text{ref}}$, combining (60) and (61), the reduced order dynamics become

$$\begin{aligned}\dot{\theta} &= \omega(p) + Z(\theta, p, y_{\text{ref}})(u - p) - \epsilon\tilde{Z}(\theta, p, y_{\text{ref}})g(x_{\text{ref}}, y_{\text{ref}}),\\ \dot{p} &= I(\theta, p, y_{\text{ref}})(u - p) - \epsilon\tilde{I}(\theta, p, y_{\text{ref}})g(x_{\text{ref}}, y_{\text{ref}}),\\ \dot{y}_{\text{ref}} &= \epsilon g(x_{\text{ref}}, y_{\text{ref}}),\end{aligned} \tag{62}$$

where $\omega(p) = 2\pi/T(p)$ and $(x_{\text{ref}}, y_{\text{ref}})$ provide a good approximation for $(x, y)$. The original equation (53) has $N+k$ states, while the reduced order equation (62) has $2+k$ states. Also notice that in the limit in which $\epsilon \to 0$ the corrections from the slow dynamics become negligible and (62) relaxes to (27) with a constant $y_{\text{ref}}$.

This general approach is illustrated for the Hodgkin–Huxley model with minor modifications described in panel A of Figure 1.10 from [21] so that the model exhibits elliptic bursting mediated by the slow variable $h$. Specifically, all equations and parameters are identical to those given in Appendix B with the exception that $\alpha_n$ and $g_{\text{Na}}$ are decreased by half, $\alpha_h$ is increased by a factor of 4, $\beta_n = 0.125\exp(-V/10)$, and the equation for $\dot{h}$ is multiplied by 0.008 so that $h$ is the slow variable. With these modifications, as shown in Figure 9, the model displays elliptic bursting with a period of approximately 1000ms with $h \in [0.41, 0.7]$. Following the fast/slow formulation from (53), $x = \begin{bmatrix} V & n & m \end{bmatrix}^T$, $y = h$, and $u = I_{\text{ext}}$. Reference trajectories $x_{\text{ref}}(\theta, p, h)$ are obtained with a strategy similar to the one described in section 4.2: choosing an $h \in [0.40, 0, 7]$ the value of $I_{\text{ext}}$ at which the Hopf bifurcation occurs, $I_H(h)$, is computed; for $p > I_H(h)$, the resulting periodic orbit is taken to be $x_{\text{ref}}(\theta, p, h)$; for $p < I_H(h)$ the initial conditions for the reference trajectories are chosen so that $\frac{\partial x_{\text{ref}}}{\partial p}$ is continuous. Likewise, the time scaling for $p < I_H(h)$ is taken to be $T(p) = T(I_H(h)) + (p - I_H(h))T'(I_H(h))$, where $'$ is the derivative with respect to $p$ so that $T(p)$ is continuously differentiable. This process is repeated for multiple constant values of $h$ in order to numerically approximate the necessary partial derivatives from (61). $Z$, $I$, $\tilde{Z}$, and $\tilde{I}$ are computed as defined in (26) taking

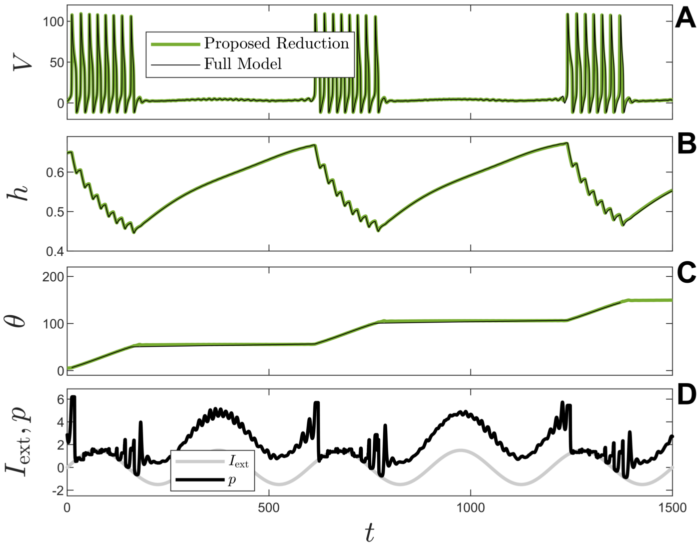

**Figure 10.** *Reduction of a model with elliptic bursting with both fast and slow variable dynamics. As described in the text, a reduced order model of the form (62) is obtained for the Hodgkin–Huxley model equations from Appendix B, modified so that $h$ is a slow variable. Panels A, B, and C give a comparison between the full and reduced order models with near-perfect agreement. For the simulation of (62), panel D compares traces of $I_{\mathrm{ext}}$ and $p$. Transitions between spiking and quiescence are preceded by rapidly growing oscillations in $p$.*

$\alpha = 0.4$. In order to avoid infinitely large values of $I$ and $Z$, when taking the pseudoinverse in this computation, all singular values smaller than 0.005 are truncated.

A representative simulation of the resulting reduced order model (62) in response to the input $I_{\mathrm{ext}} = 1.5\sin(2\pi t/300) + \sqrt{2D}\eta(t)$ is shown in Figure 10. Here $\eta(t)$ is a zero-mean white noise process where $D = 0.002$ sets the noise intensity. This additional small magnitude white noise process is added so that the model transitions through the subcritical Hopf bifurcation from quiescence to firing more quickly. Panels A, B, and C show that the transmembrane voltage, slow variable, and phase, respectively, are nearly identical between the reduced order model and the full Hodgkin–Huxley model. Simulations are performed using the Euler–Mayamara method [13]. For the full order model, the phase is inferred by incrementing the phase by $2\pi$ at every action potential and linearly interpolating at all intermediate times. Panel D shows the parameter $p$ plotted against $I_{\mathrm{ext}}$. These values are similar to each other in the spiking regime but settle to a constant offset in the quiescent regime. Note that in the absence of noise (i.e., taking $D = 0$), transition from quiescence to spiking is delayed moderately for the full model but only slightly for the reduced order model; this can likely be attributed to the fact that interpolation errors in the reduced order model perturb the system away from the unstable fixed point once the threshold for the Hopf bifurcation has been crossed.

## 5. Future considerations for the development of reduced order models for fold/homoclinic bursters (square wave bursters).

Sections 3 and 4 illustrate strategies for reduced order modeling of parabolic and elliptic bursters. A third commonly observed topological class of bursting is known as square wave bursting, where resting stability is lost as the result of a saddle-node bifurcation and spiking is subsequently arrested as the result of

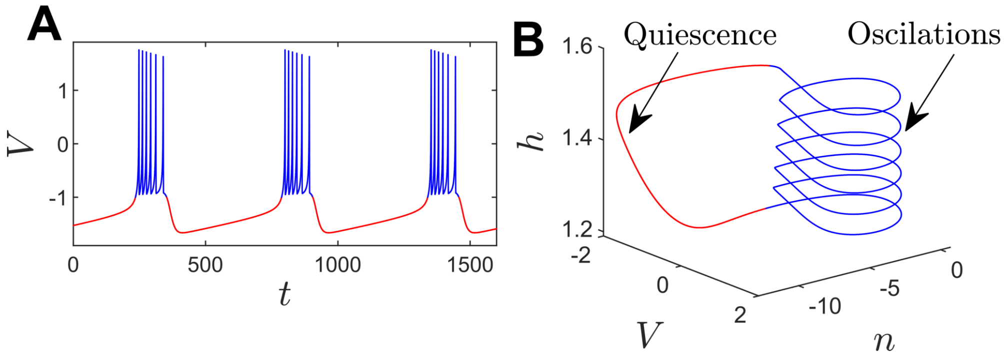

**Figure 11.** *The Hindmarsh–Rose model from* (63) *displays square wave bursting. Panel A gives a trace $V$ versus time, and panel B shows the same trajectory plotted in three dimensions. The key difficulty in developing reduced order modeling strategies for square wave bursters (as well as for other topological classifications of bursters) is that the quiescent regime (shown in red) is located in a different region of phase space from the periodically firing regime (shown in blue). Future work will consider the development of strategies to capture the transition between these two regimes.*

a saddle homoclinic orbit bifurcation. The Hindmarsh–Rose model [15] is a canonical model that exhibits square wave bursting

$$\begin{aligned} \dot{V} &= n - V^3 + bV^2 - h + I, \\ \dot{n} &= c - dV^2 - n, \\ \dot{h} &= r(s(V - V_r) - h). \end{aligned} \tag{63}$$

This model can be viewed as a phenomenological representation of the Hodgkin–Huxley equations. Here, $V$ is a dimensionless transmembrane potential, $n$ is an auxiliary variable, $h$ modulates the adaptation current, and $I = 1.4$ represents a constant baseline current. Other parameters are taken to be $s = 4, V_r = -1.6, b = 3, c = 1, d = 5$, and $r = 10^{-3}$. Allowing transients to decay, the system settles to a stable bursting limit cycle shown in Figure 11. Panel A shows $V$ as a function of time, and panel B shows the evolution in three dimensions.

A key aspect of the square-wave bursting displayed by the model (63) is that the spiking and quiescent regimes exist in different regions of phase space. This is different from parabolic bursters, where the invariant circle persists in the quiescent state. For elliptic bursters, the transition between the limit cycle and the stable fixed point is handled by carefully choosing an appropriate set of reference trajectories, $x_{\text{ref}}$, and defining reduced order variables $\theta$ and $p$ to accommodate the transition between attractors. It is conceivable that a similar approach of choosing a reference set of trajectories to capture the transition between spiking and quiescence for square wave bursters could be implemented. Note, however, that care would need to be taken in the definition of the associated reduced order coordinates so that the characteristics of the fixed points and periodic orbits of the fast equations are preserved under this transformation. The development of reduced order modeling strategies for other types of neural bursters will be the subject of future work.

## 6. Discussion and conclusion.

This work considers the development and analysis of phase-based model order reduction techniques for both parabolic and elliptic bursting neurons. In contrast to strategies that exploit separation of fast and slow timescales [3], [53], [38], [24],

[2], or use standard phase-based reduction techniques [44], [30], the proposed model order reduction strategies can accurately capture the transition between bursting and spiking regimes in response external forcing such as an applied transmembrane current or synaptic current from an upstream neuron. Future work will use these reduction techniques to investigate emergent behaviors in coupled networks of bursting neurons.

The dynamical mechanisms responsible for the transition from quiescence to bursting are different for the two topological classes of neurons considered in this work, necessitating the use of different reduction approaches. For parabolic bursters, the fast variables remain close to an invariant circle in both quiescence and firing. This allows for the definition of an extended phase as a function of both the fast and slow variables and ultimately the straightforward implementation of the extend phase reduction [26] as described in section 3. For elliptic bursters, the dynamics can be considered relative to a carefully chosen set of reference trajectories as described in section 4. Provided that the dynamics are rapidly contracting in some directions, as gauged by the eigenvalues of the Jacobian evaluated locally along trajectories, the resulting reduced order model (27) has both periodic orbits and fixed points (reflecting periodic firing and quiescence, respectively) and accurately captures the transition between the two regimes.

The approaches used in this work are different from methods that use contraction theory [27], [51] or master stability functions [36], [47]. In the approaches proposed in this work, the errors between the full order and reduced order models will generally accumulate over time, while techniques that involve contraction theory or master stability functions are typically focused on the the asymptotic convergence of a state to some underlying trajectory or attractor. Error accumulation is generally unavoidable when considering reduced order modeling of oscillatory systems owing to the unity Floquet multiplier present in all periodic orbits. The reduced order modeling approach for elliptic neurons is related to the strategy considered in [55]. The main difference between these two approaches is that the proposed strategy considers the local decay of reference solutions (as gauged by the Jacobian evaluated along trajectories), while the strategy in [55] considers the aggregate decay (as determined by the state transition matrix) to define the set of reduced order coordinates and ultimately arrive at a reduction. This subtle distinction is important for the purposes of implementation; the approach from [55] struggles when the eigenvalues of the state transition matrix are not continuous with respect to parameter perturbations, ultimately necessitating the approach described in section 4.

These reduced order modeling strategies for parabolic and elliptic bursting neurons are promising and serve as a starting point for further development of phase-based reduced order modeling for bursting neurons. However, there are still many questions to investigate. In [20], Izhikevich identified 120 different topological classes of bursting neurons that result from codimension-1 bifurcations. Through the use of fast-slow decomposition and bifurcation analysis of the resulting fast dynamics [22], [12], the mechanisms that underlie the transition between spiking and quiescence are well understood for the codimension-1 bursters (and many of the codimension-2 bursters). Nonetheless, general mathematical strategies for studying the dynamics of coupled bursters have been slow to materialize, with analytical studies confined to relatively low-dimensional phenomenological models [1], [7], [48], [43], [40], [41], [19]. The results contained in this work represent a step towards addressing the gap for two common classes of bursters. The key challenge for other types of bursters will be in the definition of an appropriate reduced order coordinate system that can accurately capture the transitions between firing and quiescence. Insight gained from the approaches presented here can serve as a starting point for the continued development of reduced order modeling techniques for other topological classes of neural bursters.

**Appendix A. Neural model for Circle/Circle bursting.** In this work, the conductance-based neural model presented in [8] is used when considering Circle/Circle bursting. This model has six state variables with relevant dynamical equations given below:

$$
\begin{aligned}
C_m\dot{V} &= I_{\mathrm{Na}} + I_{\mathrm{K}} + I_{\mathrm{Cl}} + I_{\mathrm{ext}}(t),\\
\dot{n} &= \phi\left[\alpha_n(1-n) - \beta_n n\right],\\
\dot{h} &= \phi\left[\alpha_h(1-h) - \beta_h h\right],\\
\dot{[\mathrm{Ca}]}_{\mathrm{i}} &= -0.002 g_{\mathrm{Ca}}(V - V_{\mathrm{Ca}})/\left[1+\exp(-(V+25)/2.5)\right] - [\mathrm{Ca}]_{\mathrm{i}}/80,\\
\dot{[\mathrm{K}]}_o &= -1.55 I_K - 2\beta I_{\mathrm{pump}} - I_{\mathrm{glia}} - I_{\mathrm{diff}},\\
\dot{[\mathrm{Na}]}_{\mathrm{i}} &= \frac{1.55}{\beta} I_{\mathrm{Na}} - 3I_{\mathrm{pump}}.
\end{aligned} \tag{A1}
$$

Here, $V$ represents the transmembrane voltage of the neuron, $C_m$ represents the cell membrane capacitance, $n$ and $h$ are gating variables, $[\mathrm{Ca}]_{\mathrm{i}}$, $[\mathrm{Na}]_{\mathrm{i}}$, and $[\mathrm{K}]_{\mathrm{o}}$ represent intracellular calcium, intracellular sodium, and extracellular potassium concentrations, respectively, and $I_{\mathrm{ext}}$ is a external current that could, for instance, account for the influence of synaptic current or a direct current injection from a patch clamp. In the equations for the potassium and sodium concentrations, the factor 0.31 mM $\mathrm{cm}^2/\mu$coul converts current density to rate-of-change of concentration. In this work, the variables $[\mathrm{K}]_{\mathrm{o}}$ and $[\mathrm{Na}]_{\mathrm{i}}$ are taken to be slow variables with the remaining variables comprising the fast equations. Supporting ionic functions are

$$
\begin{aligned}
I_{\mathrm{Na}} &= -g_{\mathrm{Na}} m_\infty^3 h\,(V - V_{\mathrm{Na}}) - g_{\mathrm{Na}}(V - V_{\mathrm{Na}}),\\
I_{\mathrm{K}} &= -\left(g_{\mathrm{K}} n^4 + \frac{g_{\mathrm{AHP}}[\mathrm{Ca}]_{\mathrm{i}}}{1+[\mathrm{Ca}]_{\mathrm{i}}}\right)(V - V_{\mathrm{K}}\ ) - g_{\mathrm{L}}(V - V_{\mathrm{K}}\ ),\\
I_{\mathrm{Cl}} &= -g_L(V - V_L),\\
I_{\mathrm{diff}} &= \epsilon([\mathrm{K}]_{\mathrm{o}} - \mathrm{k}_{\mathrm{o},\infty}),\\
I_{\mathrm{pump}} &= \left(\frac{\rho}{1+\exp((25-[\mathrm{Na}]_{\mathrm{i}})/3)}\right)\left(\frac{1}{1+\exp(5.5-[\mathrm{K}]_{\mathrm{o}})}\right),\\
I_{\mathrm{glia}} &= \frac{G_{\mathrm{glia}}}{1+\exp((18-[\mathrm{K}]_{\mathrm{o}})/2.5)},\\
V_{\mathrm{Na}} &= 26.64\log\left(\frac{[\mathrm{Na}]_{\mathrm{o}}}{[\mathrm{Na}]_{\mathrm{i}}}\right),\\
V_{\mathrm{K}} &= 26.64\log\left(\frac{[\mathrm{K}]_{\mathrm{o}}}{[\mathrm{K}]_{\mathrm{i}}}\right),\\
[\mathrm{Na}]_{\mathrm{o}} &= 144 + \beta(18.0 - [\mathrm{Na}]_{\mathrm{i}}),\\
[\mathrm{K}]_{\mathrm{i}} &= 140 + (18.0 - [\mathrm{Na}]_{\mathrm{i}}).
\end{aligned} \tag{A2}
$$

Supporting rate equations are

$$\begin{aligned} m_\infty &= \alpha_m/(\alpha_m+\beta_m),\\ \alpha_m &= 0.1(V+30)/(1-\exp(-0.1(V+30))),\\ \beta_m &= 4\exp(-(V+55)/18),\\ \alpha_n &= 0.01(V+34)/(1-\exp(-0.1(V+34))),\\ \beta_n &= 0.125\exp(-(V+44)/80),\\ \alpha_h &= 0.07\exp(-(V+44)/20),\\ \beta_h &= 1/(1+\exp(-0.1(V+14)))). \end{aligned} \tag{A3}$$

Other constants are as follows: $C_m = 1\mu\mathrm{F/cm}^2, g_{\mathrm{AHP}} = 0.01\mathrm{mS/cm}^2, \mathrm{g}_{\mathrm{Na}} = 100\mathrm{mS/cm}^2, \mathrm{g}_{\mathrm{K}} = 40\mathrm{mS/cm}^2, \mathrm{g}_{\mathrm{L}} = 0.05\mathrm{mS/cm}^2, \mathrm{g}_{\mathrm{Na}} = 0.0175\mathrm{mS/cm}^2, \phi = 3\mathrm{s}^{-1}, \mathrm{V}_{\mathrm{L}} = -81.93\mathrm{mV}, \mathrm{g}_{\mathrm{Ca}} = 0.1\mathrm{mS/cm}^2, \mathrm{V}_{\mathrm{Ca}} = 120\mathrm{mV}, \beta = 7, \rho = 5\mathrm{mM/s}, \mathrm{k}_{\mathrm{o},\infty} = 8\mathrm{mM}, \epsilon = 20/3\mathrm{s}^{-1}, \mathrm{G}_{\mathrm{glia}} = 333\mathrm{mM/s}$.

**Appendix B. Hodgkin–Huxley model equations.** The Hodgkin–Huxley model equations [16] and associated parameters used in this work are provided below:

$$\begin{aligned} C_m\dot{V} &= -g_{\mathrm{Na}}m^3h(V-V_{\mathrm{Na}}) - g_{\mathrm{K}}n^4(V-V_{\mathrm{K}}) - g_{\mathrm{L}}(V-V_{\mathrm{L}}) + I_{\mathrm{ext}}(t),\\ \dot{n} &= \alpha_n(1-n)-\beta_n n,\\ \dot{m} &= \alpha_m(1-m)-\beta_m m,\\ \dot{h} &= \alpha_h(1-h)-\beta_h h, \end{aligned} \tag{B1}$$

where $V$ is the transmembrane potential, and $n$, $m$, and $h \in [0,1]$ are gating variables. Maximal membrane conductances are

$$\begin{aligned} g_{\mathrm{Na}} &= 120\,\mathrm{mS/cm}^2,\\ g_{\mathrm{K}} &= 36\,\mathrm{mS/cm}^2,\\ g_{\mathrm{L}} &= 0.3\,\mathrm{mS/cm}^2, \end{aligned} \tag{B2}$$

with

$$\begin{aligned} V_{\mathrm{Na}} &= 115\,\mathrm{mV},\\ V_{\mathrm{K}} &= -12\,\mathrm{mV},\\ V_{\mathrm{L}} &= 10.599\,\mathrm{mV} \end{aligned} \tag{B3}$$

being the reversal potentials of the associated ion channels. $C_m = 1\mu\mathrm{F/cm}^2$ is the membrane capacitance, and $I_{\mathrm{ext}}$ is a baseline current in $\mu\mathrm{A/cm}^2$. The rate constants are functions of the transmembrane voltage

$$\begin{aligned} \alpha_n &= 0.01(10-V)/(\exp((10-V)/10)-1),\\ \beta_n &= 0.125\exp(-V/80),\\ \alpha_m &= 0.1(25-V)/(\exp((25-V)/10)-1),\\ \beta_m &= 4\exp(-V/18),\\ \alpha_h &= 0.07\exp(-V/20),\\ \beta_h &= 1/(\exp((-V+30)/10)+1). \end{aligned} \tag{B4}$$

**Appendix C. Preservation of SNIC bifurcation in the transformation to phase coordinates.** Following the analysis from [10] and [5], consider a conductance based neuron of the general form (2). Using $x \in \mathbb{R}^N$ to denote the full system state, one can write

$$\dot{x} = F(x, p_0) + e_1^T I_{\text{ext}}(\mu), \tag{C1}$$

where $e_1 = \begin{bmatrix} 1 & 0 & \ldots & 0 \end{bmatrix}^T$, $p_0 \in \mathbb{R}^M$ is a constant collection of parameters, $\mu \in \mathbb{R}$ modulates the value of the external current $I_{\text{ext}}$, and $^T$ denotes the vector transpose. Suppose that the system (C1) has a saddle node on an invariant circle (SNIC) bifurcation at $\mu = \mu_S$ with $F(x_S, p_0) + e_1^T I_{\text{ext}}(\mu_s) = 0$. Suppose also the when $\mu > \mu_S$ the system is in the tonically firing regime. Holding $\mu$ constant at $\mu = \mu_S + \Delta\mu > \mu_S$, where $\Delta\mu = O(\epsilon^2)$ with $0 \le \epsilon \ll 1$, Taylor expansion of (C1) about the saddle node yields

$$\Delta\dot{x} = F_x \Delta x + \frac{1}{2} \begin{bmatrix} \Delta x^T H_1 \\ \vdots \\ \Delta x^T H_N \end{bmatrix} \Delta x + e_1 \frac{\partial I_{\text{ext}}}{\partial \mu} \Delta\mu, \tag{C2}$$

where $\Delta x \equiv x - x_S$, $F_x$ denotes the Jacobian, $H_k$ denotes the Hessian associated with the $k$th entry of $x$, and all partial derivatives are evaluated at the SNIC bifurcation. As discussed in [11], the dynamics of (C1) near the SNIC bifurcation can be understood in terms of the behavior associated with the zero eigenvalue of the fixed point. Specifically, let $v_S$ and $w_S$ be right and left eigenvectors of $F_x$ associated with the $\lambda_S = 0$ eigenvalue with the scaling $||v_S||_2$ and $w_S^T v_S = 1$. As in [10], the dynamics of (C2) are governed by

$$\dot{y} = k y^2 + \zeta \Delta\mu, \tag{C3}$$

where $\zeta = w_S^T e_1 \frac{\partial I_{\text{ext}}}{\partial \mu}$ and $k$ is an appropriately defined constant. A second change of coordinates $\Upsilon = ky$ yields the one-dimensional normal form of the saddle node bifurcation

$$\dot{\Upsilon} = \Upsilon^2 + k\zeta\Delta\mu. \tag{C4}$$

For $k\zeta\Delta\mu > 0$, solutions of (C4) escape to $+\infty$ in finite time. As discussed in [10], these finite time escapes to $+\infty$ correspond to a neural spike, and one can immediately reset the solution to $-\infty$ to make the system periodic with period $T = \pi/\sqrt{k\zeta\Delta\mu}$ and frequency $\omega = 2\sqrt{k\zeta\Delta\mu}$. Reference [10] immediately computes the solution to (C4), and following a transformation to phase coordinates $\theta \in [0, 2\pi)$ as defined by isochrons (3), computes the gradient of the phase along solutions according to

$$\frac{\partial\theta}{\partial\Upsilon} = \frac{2}{\omega}(1 - \cos(\theta)). \tag{C5}$$

Considering the phase response curve from (C5), the phase reduction of (C4), valid when $\mu(t) \approx \mu_S + \Delta\mu$, takes the form

$$\dot{\theta} = \omega + \frac{2k\zeta}{\omega}(1 - \cos(\theta))(\mu(t) - \mu_S - \Delta\mu). \tag{C6}$$

Of particular interest, when taking $\mu(t) = \mu_S$, one finds

$$\begin{aligned}\dot{\theta} &= \omega - \frac{2k\zeta\Delta\mu}{\omega}(1 - \cos(\theta)) \\ &= \frac{\omega}{2}(1 + \cos(\theta)),\end{aligned} \tag{C7}$$

where the second line is obtained by noting that $2k\zeta\Delta\mu = \frac{1}{2}\omega^2$. Considering (C7), we see that (C6) also has a saddle node bifurcation that occurs when taking $\mu(t) = \mu_S$.

## Appendix D. Error bounds associated with the reduction of subHopf/fold cycle bursters.

Suppose that both $||\Delta x||$ and $||u - p||$ from (21) are order $\epsilon$ terms. Assuming that the eigenvalues of $F_x$ are simple for all $x$, i.e., they have algebraic multiplicity of 1, let $(\lambda_j, v_j, w_j)$ be an eigenvalue, right eigenvector, left eigenvector triple of $F_x$ with the normalization $||v_j||_2 = w_j^T v_j = 1$. Using the coordinate transformation $y_i = w^T \Delta x$, one can write

$$\begin{aligned}\dot{y}_i &= \dot{w}_i^T \Delta x + w_i^T \dot{x}, \\ &= \dot{w}_i^T \Delta x + w^T (F_x \Delta x + r), \\ &= \dot{w}_i^T \Delta x + \lambda_i y_i + w_i^T r.\end{aligned} \tag{D1}$$

Above, the second line is obtained by substituting (21) and truncating the order $\epsilon^2$ terms. Note that $F_x$ is a function of $x(t)$, requiring the time derivative of $w_i$ in (23). Starting with the relation $|y_i|^2 = y_i^* y_i$ where $^*$ denotes the complex conjugate, taking time derivatives, one can write

$$2|y_i|\dot{|y_i|} = y_i \dot{y}_i^* + \dot{y}_i y_i^*. \tag{D2}$$

Substituting the time derivatives from (23) into the above equation yields

$$\begin{aligned}|y_i|\dot{|y_i|} &= \mathrm{Re}(\lambda_i)|y_i|^2 + \mathrm{Re}(y_i^*(\dot{w}_i^T \Delta x + w_i^T r)) \\ &\leq \mathrm{Re}(\lambda_i)|y_i|^2 + |y_i|(||\dot{w}_i|| \cdot ||\Delta x|| + |w_i^T r|),\end{aligned} \tag{D3}$$

so that

$$\dot{|y_i|} \leq \mathrm{Re}(\lambda_i)|y_i| + ||\dot{w}_i|| \cdot ||\Delta x|| + |w_i^T r|, \tag{D4}$$

where $|| \cdot ||$ denotes the two norm. Considering the evolution of (D4) over a given time frame $t \in [t_0, t_1]$, let $\hat{\lambda}_i = \max_t(\mathrm{Re}(\lambda_i)) < 0$, $\hat{\dot{w}}_i = \max_t(||\dot{w}_i||)$, and $\hat{r}_i = \max_t(|w_i^T r_i|)$. It will be assumed that $\hat{\dot{w}}_i = O(1)$. Equation (D4) can be rewritten as

$$\dot{|y_i|} \leq \hat{\lambda}_i |y_i| + \hat{\dot{w}}_i ||\Delta x|| + \hat{r}_i. \tag{D5}$$

Considering an upper bound on $\dot{|y_i|}$, one finds that when $|y_i| \geq (-\hat{\dot{w}}_i ||\Delta x|| - \hat{r}_i)/\hat{\lambda}_i$, this implies $\dot{|y_i|} \leq 0$. As such,

$$|y_i| \leq \frac{-\hat{\dot{w}}_i ||\Delta x|| - \hat{r}_i}{\hat{\lambda}_i}, \tag{D6}$$

provided $|y_i| < (-\hat{\dot{w}}_i ||\Delta x|| - \hat{r}_i)/\hat{\lambda}_i$ at $t = 0$.

Considering (D6), if $\hat{\lambda}_i = O(1/\epsilon)$ and recalling that $\hat{\lambda}_i < 0$, i.e., with a very rapid decay, then $|y_i|$ is no larger than $O(\epsilon)$. Suppose there are a total of $\beta$ coordinates for which $\hat{\lambda}_i = O(1)$ and $N-\beta$ coordinates for which $\hat{\lambda}_i = O(1/\epsilon)$. For convenience, order $y_i$ so that $\hat{\lambda}_i \geq \hat{\lambda}_{i+1}$. With this ordering, $\hat{\lambda}_{\beta+1}, \dots, \hat{\lambda}_N$ correspond to the fast decaying directions for which the bound (D6) applies. Letting $\hat{y} = \max_{j=1\dots\beta}(|y_j|)$ and focusing on this specific coordinate with the largest magnitude, considering (D5) as a starting point, one can write

$$\begin{aligned}\dot{\hat{y}} &\leq \max_{j=1\dots\beta}(\hat{\lambda}_j)\hat{y} + \max_{j=1,\dots,\beta}(\hat{w}_j)||\Delta x|| + \max_{j=1,\dots,\beta}(\hat{r}_j)\\ &= \max_{j=1\dots\beta}(\hat{\lambda}_j)\hat{y} + \max_{j=1,\dots,\beta}(\hat{w}_j)\left|\left|\sum_{j=1}^{N} v_j y_j\right|\right| + \max_{j=1,\dots,\beta}(\hat{r}_j)\\ &= \max_{j=1\dots\beta}(\hat{\lambda}_j)\hat{y} + \max_{j=1,\dots,\beta}(\hat{w}_j)\sum_{j=1}^{N}|y_j| + \max_{j=1,\dots,\beta}(\hat{r}_j)\\ &\leq \max_{j=1\dots\beta}(\hat{\lambda}_j)\hat{y} + \max_{j=1,\dots,\beta}(\hat{w}_j)\left[\beta\hat{y} + \sum_{j=\beta+1}^{N}|y_j|\right] + \max_{j=1,\dots,\beta}(\hat{r}_j).\end{aligned} \tag{D7}$$

Note that in the second line above, $\Delta x = \sum_{j=1}^{N} v_j y_j$ and in the third line, $||\sum_{j=1}^{N} v_j y_j|| \leq \sum_{j=1}^{N} ||v_j y_j|| = \sum_{j=1}^{N} |y_j| \cdot ||v_j|| = \sum_{j=1}^{N} |y_j|$ since $||v_j|| = 1$ for all $j$. Manipulation of (D7) yields

$$\dot{\hat{y}} \leq \left[\max_{j=1\dots\beta}(\hat{\lambda}_j) + \max_{j=1,\dots,\beta}(\hat{w}_j)\beta\right]\hat{y} + \max_{j=1,\dots,\beta}(\hat{w}_j)\sum_{j=\beta+1}^{N}|y_j| + \max_{j=1,\dots,\beta}(\hat{r}_j). \tag{D8}$$

Provided $\Delta x = O(\epsilon)$ at $t=0$, for the fast decaying coordinates $y_{\beta+1}, \dots, y_N$, using (D6), one can write $|y_j| \leq -\hat{r}_j/\hat{\lambda}_j + O(\epsilon^2)$ for $j = \beta+1\dots N$. Substituting this result into (D8) and truncating $O(\epsilon^2)$ terms yields

$$\dot{\hat{y}} \leq a\hat{y} + b, \tag{D9}$$

where $a$ and $b$ are defined according to

$$\begin{aligned} a &= \max_{j=1\dots\beta}(\hat{\lambda}_j) + \max_{j=1,\dots,\beta}(\hat{w}_j)\beta,\\ b &= \max_{j=1,\dots,\beta}(\hat{w}_j)\max_{j=\beta+1,\dots,N}(-\hat{r}_j/\hat{\lambda}_j) + \max_{j=1,\dots,\beta}(\hat{r}_j).\end{aligned} \tag{D10}$$

Equation (D9) has an explicit solution

$$\hat{y}(t) = \left(\hat{y}(0) + \frac{b}{a}\right)\exp(at) - \frac{b}{a}. \tag{D11}$$

Above, note that $a$ is generally positive. Considering (D11), provided that $b = O(\epsilon)$, $\hat{y}$ remains an $O(\epsilon)$ term on $t \sim \log(1/\epsilon)$ timescales. Recalling the definition of $b$ from (D10), $b = O(\epsilon)$ when $\max_{j=1,\dots,\beta}(\hat{r}_j) = O(\epsilon)$.

## REFERENCES

[1] I. Belykh, E. De Lange, and M. Hasler, *Synchronization of bursting neurons: What matters in the network topology*, Phys. Rev. Lett., 94 (2005), 188101, https://doi.org/10.1103/PhysRevLett.94.188101.

[2] R. Bertram, M. J. Butte, T. Kiemel, and A. Sherman, *Topological and phenomenological classification of bursting oscillations*, Bull. Math. Biol., 57 (1995), pp. 413–439, https://doi.org/10.1007/BF02460633.

[3] R. E. Bertram and J. E. Rubin, *Multi-timescale systems and fast-slow analysis*, Math. Biosci., 287 (2017), pp. 105–121, https://doi.org/10.1016/j.mbs.2016.07.003.

[4] E. Brown, P. Holmes, and J. Moehlis, *Globally coupled oscillator networks*, in Perspectives and Problems in Nonlinear Science, Springer, 2003, pp. 183–215.

[5] E. Brown, J. Moehlis, and P. Holmes, *On the phase reduction and response dynamics of neural oscillator populations*, Neural Comput., 16 (2004), pp. 673–715, https://doi.org/10.1162/089976604322860668.

[6] D. Bucher, G. Haspel, J. Golowasch, and F. Nadim, *Central pattern generators*, eLS, 2015, pp. 1–12.

[7] N. Burić, K. Todorović, and N. Vasović, *Synchronization of bursting neurons with delayed chemical synapses*, Phys. Rev. E, 78 (2008), 036211, https://doi.org/10.1103/PhysRevE.78.036211.

[8] J. R. Cressmanand, G. Ullah, J. Ziburkus, S. J. Schiff, and E. Barreto, *The influence of sodium and potassium dynamics on excitability, seizures, and the stability of persistent states: I. Single neuron dynamics*, J. Comput. Neurosci., 26 (2009), pp. 159–170, https://doi.org/10.1007/s10827-008-0132-4.

[9] P. Dayan and L. F. Abbott, *Theoretical Neuroscience: Computational and Mathematical Modeling of Neural Systems*, MIT Press, Cambridge, MA, 2005.

[10] B. Ermentrout, *Type* I *membranes, phase resetting curves, and synchrony*, Neural Comput., 8 (1996), pp. 979–1001, https://doi.org/10.1162/neco.1996.8.5.979.

[11] G. B. Ermentrout and N. Kopell, *Parabolic bursting in an excitable system coupled with a slow oscillation*, SIAM J. Appl. Math., 46 (1986), pp. 233–253, https://doi.org/10.1137/0146017.

[12] G. B. Ermentrout and D. H. Terman, *Mathematical Foundations of Neuroscience*, Interdiscip. Appl. Math. 35, Springer, New York, 2010.

[13] C. W. Gardiner, *Handbook of Stochastic Methods: For Physics, Chemistry and the Natural Sciences*, Springer, Berlin, 2004.

[14] J. Guckenheimer, *Isochrons and phaseless sets*, J. Math. Biol., 1 (1975), pp. 259–273, https://doi.org/10.1007/BF01273747.

[15] J. L. Hindmarsh and R. M. Rose, *A model of neuronal bursting using three coupled first order differential equations*, Proc. Roy. Soc. Lond. Ser. B. Biol. Sci., 221 (1984), pp. 87–102.

[16] A. L. Hodgkin and A. F. Huxley, *A quantitative description of membrane current and its application to conduction and excitation in nerve*, J. Physiol., 117 (1952), pp. 500–544, https://doi.org/10.1113/jphysiol.1952.sp004764.

[17] A. B. Holt, D. Wilson, M. Shinn, J. Moehlis, and T. I. Netoff, *Phasic burst stimulation: A closed-loop approach to tuning deep brain stimulation parameters for Parkinson's disease*, Plos Comput. Biol., 12 (2016), e1005011, https://doi.org/10.1371/journal.pcbi.1005011.

[18] F. C. Hoppensteadt and E. M. Izhikevich, *Weakly Connected Neural Networks*, Springer, New York, 1997.

[19] M. V. Ivanchenko, G. V. Osipov, V. D. Shalfeev, and J. Kurths, *Phase synchronization in ensembles of bursting oscillators*, Phys. Rev. Lett., 93 (2004), 134101, https://doi.org/10.1103/PhysRevLett.93.134101.

[20] E. M. Izhikevich, *Neural excitability, spiking and bursting*, Internat. J. Bifur. Chaos, 10 (2000), pp. 1171–1266, https://doi.org/10.1142/S0218127400000840.

[21] E. M. Izhikevich, *Synchronization of elliptic bursters*, SIAM Rev., 43 (2001), pp. 315–344, https://doi.org/10.1137/S0036144500382064.

[22] E. M. Izhikevich, *Dynamical Systems in Neuroscience: The Geometry of Excitability and Bursting*, MIT Press, Cambridge, MA, 2007.

[23] D. Jordan and P. Smith, *Nonlinear Ordinary Differential Equations: An Introduction for Scientists and Engineers*, 4th ed., Oxford University Press, Oxford, 2007.

[24] T. B. Kepler, L. F. Abbott, and E. Marder, *Reduction of conductance-based neuron models*, Biol. Cybernet., 66 (1992), pp. 381–387, https://doi.org/10.1007/BF00197717.

[25] Y. Kuramoto, *Chemical Oscillations, Waves, and Turbulence*, Springer-Verlag, Berlin, 1984.

[26] W. Kurebayashi, S. Shirasaka, and H. Nakao, *Phase reduction method for strongly perturbed limit cycle oscillators*, Phys. Rev. Lett., 111 (2013), 214101, https://doi.org/10.1103/PhysRevLett.111.214101.

[27] W. Lohmiller and J. J. E. Slotine, *On contraction analysis for non-linear systems*, Automatica, 34 (1998), pp. 683–696, https://doi.org/10.1016/S0005-1098(98)00019-3.

[28] E. Marder and D. Bucher, *Central pattern generators and the control of rhythmic movements*, Curr. Biol., 11 (2001), pp. R986–R996, https://doi.org/10.1016/S0960-9822(01)00581-4.

[29] E. Marder, D. Bucher, D. J. Schulz, and A. L. Taylor, *Invertebrate central pattern generation moves along*, Curr. Biol., 15 (2005), pp. R685–R699, https://doi.org/10.1016/j.cub.2005.08.022.

[30] A. Mauroy, B. Rhoads, J. Moehlis, and I. Mezić, *Global isochrons and phase sensitivity of bursting neurons*, SIAM J. Appl. Dyn. Syst., 13 (2014), pp. 306–338, https://doi.org/10.1137/130931151.

[31] B. Monga, D. Wilson, T. Matchen, and J. Moehlis, *Phase reduction and phase-based optimal control for biological systems: A tutorial*, Biol. Cybernet., 113 (2019), pp. 11–46, https://doi.org/10.1007/s00422-018-0780-z.

[32] S. Moran, S. M. Moenter, and A. Khadra, *A unified model for two modes of bursting in GnRH neurons*, J. Comput. Neurosci., 40 (2016), pp. 297–315, https://doi.org/10.1007/s10827-016-0598-4.

[33] C. A. Del Negro, S. M. Johnson, R. J. Buteraand, and J. C. Smith, *Models of respiratory rhythm generation in the pre-Bötzinger complex.* III. *Experimental tests of model predictions*, J. Neurophysiol., 86 (2001), pp. 59–74, https://doi.org/10.1152/jn.2001.86.1.59.

[34] T. Netoff, M. A. Schwemmer, and T. J. Lewis, *Experimentally estimating phase response curves of neurons: Theoretical and practical issues*, in Phase Response Curves in Neuroscience, Springer, 2012, pp. 95–129.

[35] C. Park and J. E. Rubin, *Cooperation of intrinsic bursting and calcium oscillations underlying activity patterns of model pre-Bötzinger complex neurons*, J. Comput. Neurosci., 34 (2013), pp. 345–366, https://doi.org/10.1007/s10827-012-0425-5.

[36] L. M. Pecora and T. L. Carroll, *Master stability functions for synchronized coupled systems*, Phys. Rev. Lett., 80 (1998), pp. 2109–2112, https://doi.org/10.1103/PhysRevLett.80.2109.

[37] B. Pietras and A. Daffertshofer, *Network dynamics of coupled oscillators and phase reduction techniques*, Phys. Rep., 819 (2019), pp. 1–105.

[38] J. Rinzel, *Bursting oscillations in an excitable membrane model*, in Ordinary and Partial Differential Equations: Proceedings of the Eighth Conference held at Dundee, Scotland, Springer, 1985, pp. 304–316.

[39] C. B. Roberts, M. P. O'Boyle, and K. J. Suter, *Dendrites determine the contribution of after depolarization potentials (ADPs) to generation of repetitive action potentials in hypothalamic gonadotropin releasing-hormone (GnRH) neurons*, J. Comput. Neurosci., 26 (2009), pp. 39–53, https://doi.org/10.1007/s10827-008-0095-5.

[40] N. F. Rulkov, *Regularization of synchronized chaotic bursts*, Phys. Rev. Lett., 86 (2001), pp. 183–186, https://doi.org/10.1103/PhysRevLett.86.183.

[41] N. F. Rulkov, *Modeling of spiking-bursting neural behavior using two-dimensional map*, Phys. Rev. E, 65 (2002), 041922, https://doi.org/10.1103/PhysRevE.65.041922.

[42] J. A. Sanders, F. Verhulst, and J. Murdock, *Averaging Methods in Nonlinear Dynamical Systems*, 2nd ed., Springer-Verlag, New York, 2007.

[43] Y. Shen, Z. Hou, and H. Xin, *Transition to burst synchronization in coupled neuron networks*, Phys. Rev. E, 77 (2008), 031920, https://doi.org/10.1103/PhysRevE.77.031920.

[44] W. E. Sherwood and J. Guckenheimer, *Dissecting the phase response of a model bursting neuron*, SIAM J. Appl. Dyn. Syst., 9 (2010), pp. 659–703, https://doi.org/10.1137/090773519.

[45] J. C. Smith, H. H. Ellenbergerand, K. Ballanyi, D. W. Richter, and J. L. Feldman, *Pre-Bötzinger complex: A brainstem region that may generate respiratory rhythm in mammals*, Science, 254 (1991), pp. 726–729, https://doi.org/10.1126/science.1683005.

[46] R. B. Stein, *Some models of neuronal variability*, Biophys. J., 7 (1967), pp. 37–68, https://doi.org/10.1016/S0006-3495(67)86574-3.

[47] J. Sun, E. M. Bollt, and T. Nishikawa, *Master stability functions for coupled nearly identical dynamical systems*, Europhys. Lett., 85 (2009), 60011, https://doi.org/10.1209/0295-5075/85/60011.

[48] X. Sun, J. Lei, M. Perc, J. Kurths, and G. Chen, *Burst synchronization transitions in a neuronal network of subnetworks*, Chaos, 21 (2011), 016110, https://doi.org/10.1063/1.3559136.

[49] H. C. Tuckwell, *Introduction to Theoretical Neurobiology: Linear Cable Theory and Dendritic Structure*, Vol. 1, Cambridge University Press, Cambridge, 1988.

[50] C. Van Vreeswijk, L. F. Abbott, and G. B. Ermentrout, *When inhibition not excitation synchronizes neural firing*, J. Comput. Neurosci., 1 (1994), pp. 313–321, https://doi.org/10.1007/BF00961879.

[51] W. Wang and J.-J. E. Slotine, *On partial contraction analysis for coupled nonlinear oscillators*, Biol. Cybernet., 92 (2005), pp. 38–53, https://doi.org/10.1007/s00422-004-0527-x.

[52] Y. Wang, J. P. Gill, H. J. Chiel, and P. J. Thomas, *Shape versus timing: Linear responses of a limit cycle with hard boundaries under instantaneous and static perturbation*, SIAM J. Appl. Dyn. Syst., 20 (2021), pp. 701–744, https://doi.org/10.1137/20M1344974.

[53] Y. Wang and J. E. Rubin, *Complex bursting dynamics in an embryonic respiratory neuron model*, Chaos, 30 (2020), 043127, https://doi.org/10.1063/1.5138993.

[54] D. Wilson, *An adaptive phase-amplitude reduction framework without $\mathcal{O}(\epsilon)$ constraints on inputs*, SIAM J. Appl. Dyn. Syst., 21 (2022), pp. 204–230, https://doi.org/10.1137/21M1391791.

[55] D. Wilson, *A reduced order modeling framework for strongly perturbed nonlinear dynamical systems near arbitrary trajectory sets*, SIAM J. Appl. Dyn. Syst., 22 (2023), pp. 603–634, https://doi.org/10.1137/21M1451154.

[56] D. Wilson and J. Moehlis, *Clustered desynchronization from high-frequency deep brain stimulation*, PLoS Comput. Biol., 11 (2015), e1004673, https://doi.org/10.1371/journal.pcbi.1004673.

[57] A. Winfree, *The Geometry of Biological Time*, 2nd ed., Springer Verlag, New York, 2001.

[58] A. T. Winfree, *Biological rhythms and the behavior of populations of coupled oscillators*, J. Theoret. Biol., 16 (1967), pp. 15–42, https://doi.org/10.1016/0022-5193(67)90051-3.